Absolute cross sections for electron loss, electron capture, and multiple ionization in collisions of C^{3+} with noble gases

A. C. F. Santos,[1] G. M. Sigaud,[2,*] W. S. Melo,[3] M. M. Sant'Anna,[1] and E. C. Montenegro[1]

[1]*Instituto de Física, Universidade Federal do Rio de Janeiro, Caixa Postal 68528, Rio de Janeiro, RJ 21945-970, Brazil*

[2]*Departamento de Física, Pontifícia Universidade Católica do Rio de Janeiro, Caixa Postal 38071, Rio de Janeiro, RJ 22452-970, Brazil*

[3]*Departamento de Física, Universidade Federal de Juiz de Fora, Juiz de Fora, MG 36036-330, Brazil*

(Received 28 April 2010; published 14 July 2010)

Absolute charge-state-correlated cross sections for projectile electron loss, electron capture, and target multiple ionization in collisions between C^{3+} ions and noble gases have been measured for energies between 1.3 and 3.5 MeV. The data have been compared with other similar absolute cross sections existent in the literature for several projectiles. Calculations for the single-loss−multiple-ionization channel have been performed for the screening mode, using both an extended version of the classical-impulse free-collision model and the plane-wave Born approximation (PWBA), and for the antiscreening mode within the PWBA. The energy dependence of the average number of target active electrons which contribute to the antiscreening has been described by means of a simple function, which is "universal" for noble gases but, in principle, projectile dependent. A method has been developed to obtain the number of active target electrons for each subshell in the high-velocity regime, which presented physically reasonable results. Analyses of the dependences of the single-capture and transfer-ionization (SC and TI, respectively) processes on the projectile charge states showed that, for He, equally charged bare and dressed projectiles have very similar cross sections; the latter thus acting as structureless point charges. A behavior similar to that in the SC has been observed for the pure single ionization of He by projectiles with different charge states and of the other noble gases by singly charged projectiles. It has been shown that the q^2 dependence of the pure-single and total-ionization cross sections, predicted by first-order models, is only valid for high-collision velocities. For slower collisions, the electron capture process becomes more relevant and competes with the ionization channel, a feature which grows in importance as the projectile charge state increases.

DOI: 10.1103/PhysRevA.82.012704 PACS number(s): 34.50.Fa, 52.20.Hv

I. INTRODUCTION

One of the most important processes in atomic collisions in the low- to intermediate-velocity regime is the multiple ionization of atoms by dressed ions due to the wide range of applications in many fields, such as plasma physics [1], accelerator technology [2], planetary atmospheres [3], radiotherapy and radiation dosimetry [4], heavy-ion-beam materials modification and analysis [5], and nuclear fusion [6,7]. From the point of view of fundamental physics, this process has intrinsic scientific interest because it involves a variety of complex competing processes which may occur simultaneously with the target ionization—such as electron loss and capture by the projectile—besides the direct-ionization channel, presenting theoretical and experimental challenges, many of them not yet overcome. In this velocity region, the time-dependent dynamics of many-electron systems can seldom be described by perturbative models, especially in the case when the projectile ion also carries electrons [8–10].

Multiple ionization is, in itself, a complex process to describe, due to the fact that there are several possible pathways through which it may occur. The simplest case, namely, that of double ionization by swift ions, for instance, can be quite well understood in terms of four mechanisms [11,12]: (i) a shake-off process, where one electron is ionized directly by the projectile, with a second electron being ejected by a rearrangement in the final state; (ii) the ionization of one electron which, on its way out of the target, knocks out the second electron; (iii) the direct ionization of an inner-shell electron by the projectile, followed by a postcollisional Auger-like ionization; and (iv) the ionization of two electrons by the direct interaction with the projectile in the same collision. The cross sections for the first three processes are essentially proportional to the single-ionization cross section, while those for the latter—which is the dominant process in the low- to intermediate-velocity region [13]—depend on the projectile velocity and charge state quite differently than the single-ionization ones. However, even in this case, the dependences of the cross sections on the projectile charge states and/or the influence of competitive collision channels can be quite strong, as has been shown for the ratio between double and single ionization of the He target with and without the simultaneous electron loss or capture by dressed C and/or O projectile ions, in the low- to intermediate-velocity regime [14–18].

When more than two target electrons are removed, the problem becomes increasingly more complex, due not only to the nonlinear increase in the possible ways to reach a given target charge state but also to the crescent role that other competitive collision channels may play in these processes. From the theoretical point of view, probably the most widely used methods to describe the multiple ionization process lie within the framework of the independent-particle model (IPM), where it is assumed that the target electrons are ionized independently of each other and the different ionization probabilities are combined to provide the total cross sections by means of the binomial and multinomial distributions [10,19–24]. This approach has been also used, for instance, to take into account postcollisional time-delayed ionization of the target with quite successful results [25–30].

*gms@vdg.fis.puc-rio.br

However, these methods depend strongly on accurate calculations for the single-electron transition probabilities, which can be a very difficult task for some processes, especially in the case of electron capture.

Another approach which has been used to deal with the multiple ionization of atoms is the statistical energy deposition model [31–35], which is based on the hypothesis that the projectile deposits on the target a certain amount of energy which is statistically shared between the electrons, causing one or more of them to be ionized in a postcollisional step.

In the low- to high-velocity regime and for heavier systems, perturbative methods become less reliable and different approaches have to be used. Alternatives range from classical models, such as classical trajectory Monte Carlo methods [36–38] or the free-collision model (also called classical impulse approximation) [8,39,40], to more rigorous quantum mechanical calculations, the latter almost always restricted to collisions in which electron capture can be neglected [41–43]. Full quantum calculations which take into account the ionization of both collision partners, as well as charge transfer between them, are rare and have only very recently been done [9,10,44–46].

As concerns the experimental data, most of the available results refer to relative cross sections—that is, ratios of multiple to single cross sections (see, e.g., Refs. [14–18,47–55]). Absolute measurements of multiple-ionization cross sections are rather scarce; moreover when one looks for exclusive measurements, where the final charge states not only of the target but also of the projectile are obtained in coincidence. DuBois *et al.* [52] measured absolute multiple-ionization cross sections for noble gases from He to Kr induced by protons, in the energy range from 10 to 4000 keV, while Knudsen *et al.* [56] presented similar absolute data for He in collisions with several ions with different charge states, with energies between 0.13 and 15 MeV/amu. However, these two sets of measurements were performed without the discrimination of the projectile final state, except in the latter case for highly charged B and C ions (these results are discussed in more detail later on in this article). Shah and Gilbody [57] presented absolute measurements of single and double ionization of He by fully stripped H, He, and Li ions, with energies ranging from 50 to 2380 keV/amu, where both the direct-ionization and transfer-ionization channels were discriminated. These measurements were extended to higher energies ($E = 0.5$–12.0 MeV) by Forest *et al.* [58] for He^+ on He. DuBois performed similar measurements for H^+, He^+, and He^{2+} ions colliding with noble gases from He to Kr, covering a wide energy range (10 keV to 2 MeV) [59–63]. In the latter article, the loss-ionization channel for He^+ was also measured. And, in a previous work, DuBois and Toburen [64] reported of single and double pure ionization of the He target by several projectiles with different charge states. More recently, Woitke and co-workers [65] published absolute cross sections for the multiple ionization of He by Li^{q+} projectiles ($E/q = 0.5$–8.0 MeV/q, $q = 1$–3), where not only the loss-ionization channel but also the direct-ionization and transfer-ionization channels were measured. Cavalcanti *et al.* [25,26] have presented pure multiple-ionization cross sections of noble gases from He to Xe in collisions with protons, covering an energy range (namely, 0.75–3.50 MeV) where the capture channel is negligible. Saito and co-workers [66] have measured absolute cross sections of multiple ionization of the Ar target in coincidence with the final charge states of the projectile C^{3+} at a fixed energy of 2.0 MeV. For heavier collision partners, there is a series of publications by Tonuma and co-workers [67–69], who reported on coincidence measurements of multiply charged Ne and Ar projectiles on Ne and Ar targets at the fixed energy of 1.05 MeV/amu, where the dependences of the multiple-target ionization on the projectile charge state and on the collision channel were discussed in detail.

In a previous work, aiming to obtain more detailed data on the multiple ionization of atoms, we have measured the absolute cross sections for the pure multiple-ionization channel of noble gases from He to Xe by He^+ projectiles in the 1.0−3.5-MeV energy region [13]. Later, we have presented measurements of multiple ionization of Ne by C^{3+} ions in coincidence with the emergent charge states of the projectile in the same energy range of the previous He^+ data, thus covering the pure-ionization, transfer-ionization, and loss-ionization channels [10]. In this latter article, calculations using the basis generator method [9,10,44,45] have also been performed, showing a very good overall agreement with the experiment.

The choice of C^{3+} as a projectile is particularly interesting because, in this context, the detailed investigation of collisions between Li-like projectiles, with velocities ranging from below 1 to a few atomic units, and noble gas targets can provide useful information to increase our knowledge about charge-changing processes in a nonperturbative regime, since one can consider the $2s$ electron of these projectiles as the only active electron contributing to the projectile electron loss. Moreover, the ionization energy of the $2s$ electron of C^{3+} is not much different than that of He^+, so that one can analyze the influence of the correlation between the electron clouds of both collision partners in the loss-ionization channel. And, last but not least, Li-like projectiles, such as C^{3+}, are more efficient in the electron capture process than, for example, H^+ or He^+ in this velocity range, because of their larger effective charge.

In this article, we present measurements of absolute cross sections for the processes of pure multiple ionization, single-electron loss and single-electron capture, both accompanied by multiple target ionization, of He, Ar, Kr, and Xe targets by C^{3+} ions, in the energy range from 1.3 to 3.5 MeV. In Eqs. (1) to (3), the various processes which have been measured are shown, together with the notation for the absolute charge-changing cross sections which will be used throughout the text, namely, $\sigma_{ij}^{qq'}$, where i and j represent, respectively, the initial and final states of the target, and q and q' are the initial and final states of the projectile, respectively. Thus, the channel of target multiple ionization accompanied by projectile single-electron capture is represented by

$$P^{q+} + T^0 \rightarrow P^{(q-1)+} + T^{j+} : \sigma_{0j}^{q,q-1}, \tag{1}$$

while the process of target multiple ionization accompanied by projectile single-electron loss is given by

$$P^{q+} + T^0 \rightarrow P^{(q+1)+} + T^{j+} : \sigma_{0j}^{q,q+1}, \tag{2}$$

and the pure multiple-ionization process is described by

$$P^{q+} + T^0 \rightarrow P^{q+} + T^{j+} : \sigma_{0j}^{qq}, \tag{3}$$

TABLE I. Multiple-ionization absolute cross sections (in Mb) of He accompanied by single-electron capture by the C^{3+} projectile, as a function of the projectile energy, E.

E (MeV)	He^{+}	He^{2+}
1.3	208 ± 31	56 ± 8
1.5	139 ± 21	54 ± 8
2.0	79 ± 13	37 ± 5
2.5	38 ± 6	16 ± 2
3.0	33 ± 7	12 ± 2
3.5	18 ± 5	7.2 ± 1.2

where P and T represent the projectile and the target, respectively. In the present measurements, since the targets are neutral atoms, i is always equal to 0.

The data obtained here were compared with the other available absolute experimental results. Most of these, as pointed out previously, refer to the He target, except for the sets of data from DuBois and co-workers [52,59–63], the data from Saito *et al.* [66], and our own published data [10,13]. We have also compared our results of the single-loss−multiple-ionization channel to calculations in the plane-wave Born approximation (PWBA) [70] and the extended free-collision model [40], together with an analysis of the antiscreening contribution to the single-electron loss made following the reasoning presented by Montenegro *et al.* [71].

The article is organized as follows. In Sec. II, the general aspects of the experimental setup are briefly described. In Sec. III, the experimental results for multiple ionization of He, Ar, Kr, and Xe targets by C^{3+} for the single-capture−multiple-ionization, the single-loss−multiple-ionization, and the pure multiple-ionization channels are presented separately and compared with the existent experimental data and with calculations in the PWBA [70] and the extended free-collision model [40] for the single-loss−multiple-ionization process. Conclusions are drawn in Sec. IV. Finally, in the Appendix, all the various cross sections which appear in the discussion of the present results are defined.

II. EXPERIMENT

The experimental apparatus has been described in detail elsewhere [10,13,72] and only the most important features are presented here. Briefly, monoenergetic C^{3+} ion beams, with energies ranging from 1.3 to 3.5 MeV and an energy resolution of 1 part in 200, are obtained from C^{+} ion beams delivered by the 4-MV Van de Graaff accelerator of the Pontifical Catholic University of Rio de Janeiro, which pass through a gas stripper. The selection of charge, mass, and energy of the original beam is made by a 90° magnet, followed by a switching magnet located just after the gas stripper and before the entrance of the beam line. The beam is collimated and separated from its spurious components by a third magnet placed just before the gas cell.

After crossing the collision chamber where the gas cell is placed, the emergent beam is charge analyzed by a fourth magnet, which separates the three measured emergent charge states, C^{2+}, C^{3+}, and C^{4+}, corresponding to the electron-capture, pure-ionization and electron-loss channels, respectively. These are recorded by two surface barrier detectors located in a detection chamber placed at the end of the beam line 4 m downstream, using the same procedure as described in Ref. [10]. The multiply charged atomic recoil ions, produced by the primary beam under single-collision conditions, are accelerated by a two-stage transverse electric field and detected by two microchannel plate detectors in a chevron configuration. They provide stop signals to two time-to-amplitude converters started by the signals from the surface barrier detectors in a standard time-of-flight coincidence technique. The large and constant extraction field (960 V/cm) assures that even ions reaching the detector with substantial kinetic energy differences are collected with equal efficiency. The recoil ion detection efficiencies are obtained using the same procedure described by Santos *et al.* [13,72].

The main sources of uncertainties are due to pressure and background fluctuations (∼2%), impurities in the gas targets due to the gas-admittance system (∼1−3%), counting statistics and subtraction of random coincidences (up to ∼20%), and the effective length of the cell (∼5%). The overall uncertainties range from 15 to 30%.

III. RESULTS AND DISCUSSION

A. Single capture accompanied by target multiple ionization

The absolute cross sections for the multiple ionization of He, Ar, Kr, and Xe atoms accompanied by single-electron capture by the C^{3+} projectile, σ_{0j}^{32} with $j \neq 0$ [see Eq. (1)], are listed in Tables I to IV as functions of the projectile energy.

The largest cross sections are those for the pure single-electron capture (SC) channel—that is, the single capture with single-electron removal (ER), σ_{01}^{32},

$$C^{3+} + T^{0} \rightarrow C^{2+} + T^{+}, \tag{4}$$

TABLE II. Multiple-ionization absolute cross sections (in Mb) of Ar accompanied by single-electron capture by the C^{3+} projectile, as a function of the projectile energy, E.

E (MeV)	Ar^{+}	Ar^{2+}	Ar^{3+}	Ar^{4+}	Ar^{5+}	Ar^{6+}
1.3	152 ± 29	226 ± 38	95 ± 17	19 ± 4	6.5 ± 2.3	4.3 ± 1.5
1.5	168 ± 25	134 ± 20	68 ± 10	26 ± 4	6.9 ± 1.4	2.5 ± 0.8
2.0	84 ± 13	82 ± 12	40 ± 6	15 ± 3	9.3 ± 2.3	3.3 ± 1.0
2.5	101 ± 17	60 ± 10	15 ± 4	5.0 ± 1.0		
3.0	26 ± 4	25 ± 4	6.2 ± 1.3	2.1 ± 0.3	1.1 ± 0.2	
3.5	15 ± 4	13 ± 3	4.1 ± 1.3	1.8 ± 0.3	1.1 ± 0.2	

TABLE III. Multiple-ionization absolute cross sections (in Mb) of Kr accompanied by single-electron capture by the C^{3+} projectile, as a function of the projectile energy, E.

E (MeV)	Kr^{+}	Kr^{2+}	Kr^{3+}	Kr^{4+}	Kr^{5+}	Kr^{6+}	Kr^{7+}	Kr^{8+}
1.3	188 ± 28	261 ± 38	158 ± 22	67 ± 10	35 ± 4	22 ± 3	9.5 ± 2.2	3.5 ± 1.2
1.5	147 ± 22	150 ± 23	100 ± 15	41 ± 7	13 ± 2	8.1 ± 1.6	5.2 ± 1.6	4.6 ± 1.6
2.0	73 ± 11	85 ± 13	58 ± 9	21 ± 4	12 ± 2	11 ± 2	3.2 ± 1.0	1.3 ± 0.5
2.5	69 ± 17	47 ± 7	21 ± 3	6.5 ± 1.2	5.6 ± 1.0			
3.0	25 ± 5	26 ± 5	16 ± 3	10 ± 2	8.7 ± 2.0			
3.5	9.6 ± 2.4	9.6 ± 2.4	7.8 ± 1.7	3.0 ± 0.9	2.0 ± 0.6			

and for the transfer-ionization (TI) channel—that is, the single capture with double ER, σ_{02}^{32},

$$C^{3+} + T^{0} \rightarrow C^{2+} + T^{2+}, \tag{5}$$

where T represents a given target.

It should be noted that the TI channel dominates the SC one for the lowest velocity measured here for the Ar, Kr, and Xe targets, decreasing to the values of the SC channel as the velocity increases.

It can be seen from these tables that, in general, the differences between the cross sections σ_{0j}^{32}, for $j = 1$–4, for the Ar, Kr, and Xe targets are not large for a given energy, the values being quite similar within the experimental errors, thus indicating that the number of target electrons which are removed in the electron-capture process accompanied by target multiple ionization is quite independent of the total number of electrons in the target, at least for heavy targets and for a relatively low number of removed electrons.

In Fig. 1, the sums of the present partial cross sections for single capture accompanied by target multiple ionization for He, Ar, Kr, and Xe, together with the Ne data from Kirchner *et al.* [10], $\sigma^{32} = \sum_{j \neq 0} \sigma_{0j}^{32}$, are compared to the total single-capture cross sections of Melo *et al.* [8] for He to Xe targets, to the Ar data of Wolff *et al.* [73], to the Ar measurement of Saito *et al.* [66], and to the H-target data of Sant'Anna *et al.* [74]. Also shown in this figure are the calculations for the single-electron-capture cross sections of C^{3+} from Ne, Ar, Kr, and Xe using the semiclassical Bohr-Lindhard model as presented by Knudsen *et al.* [75]. It can be noted that the sum of the present partial cross sections are in very good agreement with the measured total cross sections for all targets. Also, the capture cross sections for the H and He targets lie systematically below the other data. However, the behavior of the total cross sections for Ar, Kr, and Xe with the collision velocity does not seem to present any noticeable dependence on the targets within the experimental errors. This may be due to the fact that all noble gases from Ne to Xe have eight electrons in their outermost subshells in an ns^2np^6 configuration, with $n = 2$–5; thus, it seems that the total single-electron-capture cross section does not depend strongly on the radial structure of the wave functions of the outermost electrons. The calculations using that simple semiclassical model provide good estimates for the single-electron capture in the intermediate-velocity regime, although they show a clear trend of increasing with the target atomic number which disagrees with the experiment. It should be noted at this point that the data presented here refer to exclusive measurements and that there is no available theoretical calculation which can be compared to the whole set of partial electron-capture cross sections.

In order to investigate the dependence of the single capture accompanied by target multiple ionization channels with the projectile charge state, the present data for the SC, $\sigma_{01}^{q,q-1}$, and the TI, $\sigma_{02}^{q,q-1}$, channels are compared in Figs. 2 to 4 for He, Ar, and Kr, respectively, with data available in the literature, for various projectiles with different charge states, as functions of the projectile velocity in atomic units, v/v_0, where v_0 is the Bohr velocity. The upper part of these figures (a) refer to the SC channel, while the lower part (b) represent the TI channel. The data in Fig. 2 are from Shah and Gilbody (H^{+}, He^{2+}, and Li^{3+} projectiles) [57], DuBois (He^{q+} projectiles, with $q = 1$, 2) [62,63], and Woitke *et al.* (Li^{q+} projectiles, with $q = 1$, 2, 3) [65]. In Figs. 3 and 4 the only other available data for Ar and Kr targets are those published by DuBois [62,63] for He^{+} and He^{2+} projectiles and the 2.0-MeV C^{3+} data for Ar from Saito *et al.* [66]. The latter data lie above the present data, a fact that also occurs for the pure multiple-ionization channel (see Figs. 19 and 20).

TABLE IV. Multiple-ionization absolute cross sections (in Mb) of Xe accompanied by single-electron capture by the C^{3+} projectile, as a function of the projectile energy, E.

E (MeV)	Xe^{+}	Xe^{2+}	Xe^{3+}	Xe^{4+}	Xe^{5+}	Xe^{6+}	Xe^{7+}	Xe^{8+}	Xe^{9+}
1.3	189 ± 24	285 ± 42	169 ± 27	63 ± 13	21 ± 5	30 ± 6	15 ± 4	9.6 ± 2.0	8.7 ± 1.9
1.5	126 ± 19	137 ± 21	84 ± 15	49 ± 10	38 ± 9	18 ± 4	14 ± 4	8.0 ± 1.7	6.8 ± 1.5
2.0	52 ± 8	56 ± 9	41 ± 8	27 ± 5	19 ± 4	13 ± 3	11 ± 3	6.3 ± 1.5	4.9 ± 1.5
2.5	24 ± 4	32 ± 5	23 ± 4	16 ± 3	13 ± 3	5.5 ± 1.2			
3.0	25 ± 4	22 ± 4	23 ± 4	22 ± 4	18 ± 4				
3.5	9.9 ± 1.7	9.9 ± 1.7	9.9 ± 1.7	7.0 ± 1.5	3.8 ± 0.8				

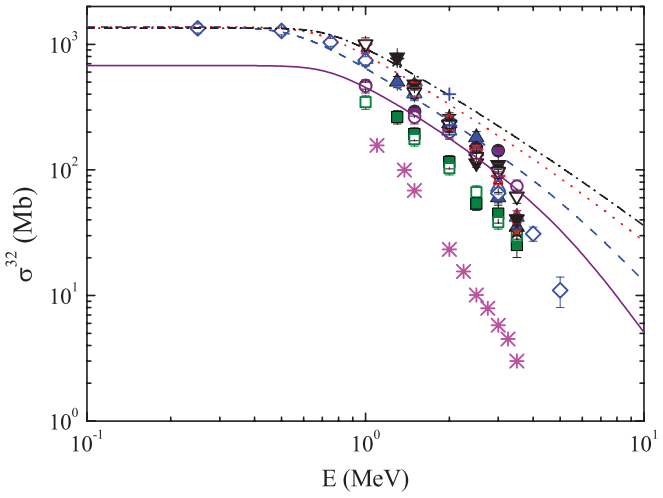

FIG. 1. (Color online) Total absolute single-electron-capture cross sections (in Mb) of C^{3+} as a function of the projectile energy in MeV. Experiment: solid symbols, sum of the partial cross sections for single capture accompanied by target multiple ionization, this work (He, green squares; Ar, blue up triangles; Kr, red stars; and Xe, black down triangles) and Ne, purple circles (Ref. [10]); open symbols: total cross sections from Ref. [8] (He, green squares; Ne, purple circles; Ar, blue up triangles; Kr, red stars; and Xe, black down triangles), Ref. [73] (Ar, blue diamonds), Ref. [74] (H, magenta asterisks), and Ref. [66] (Ar, blue cross). Theory: semiclassical Bohr-Lindhard model [75]: solid purple line, Ne; dashed blue line, Ar; dotted red line, Kr; and dash-dotted black line, Xe (see text for details).

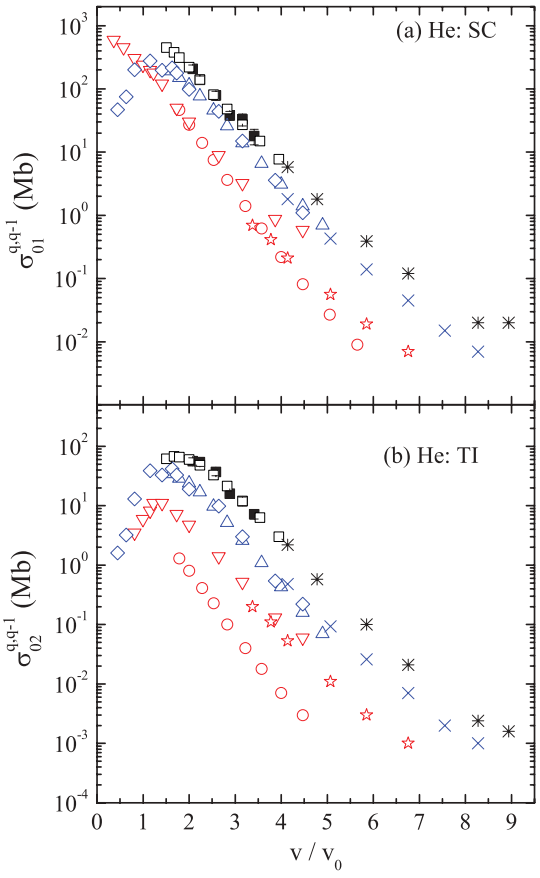

FIG. 2. (Color online) Single-capture (a) and transfer-ionization (b) channels for the He target, as functions of the projectile velocity in atomic units. Symbols: black solid squares, C^{3+}, this work; red circles, H^+, blue up triangles, He^{2+}, and black open squares, Li^{3+}, from Ref. [57]; red down triangles, He^+, from Ref. [63]; blue diamonds, He^{2+}, from Ref [62]; and red stars, Li^+, blue crosses, Li^{2+}, and black asterisks, Li^{3+}, from Ref. [65].

Some interesting points appear from the analysis of these figures. Let us first consider the He case (Fig. 2). First, it can be seen that, in the low- to intermediate-velocity region, the SC—and, to a lesser extent, also the TI—data for projectiles with the same charge state tend to coalesce. This is most notable for the SC and TI data for C^{3+} (black solid squares) and Li^{3+} projectiles (black open squares and black asterisks), which are practically the same in the velocity region where they overlap, but it also occurs for He^{2+} (blue up triangles and blue diamonds) and Li^{2+} (blue crosses), although not for the whole velocity range in the TI case. Thus, for both the SC and TI channels on He, C^{3+} ions act as pointlike projectiles with a charge equal to 3. Also, there is an ordering in the cross sections, which increase as the projectile charge state increases for the same collision velocity. This latter feature—which is expected from the semiclassical Bohr-Lindhard model for the total electron-capture cross section [75]—occurs for both the SC and TI processes. However, in the SC case, the data for the He^+ (red down triangles) and Li^+ (red stars) projectiles tend to be larger than those for protons (red circles) as the collision velocity increases. For the TI channel, the data for He^+ and Li^+ are practically the same and almost one order of magnitude larger than the corresponding proton data, for all velocities considered.

For the heavier targets, Ar and Kr, it can be seen from Figs. 3 and 4, respectively, that the behaviors of the cross sections, although similar to each other, are not the same as those for the He target. For the SC process, the data for the C^{3+} (black solid and open squares) and He^{2+} (blue triangles) projectiles are very close, being more than one order of magnitude larger than those for He^+ (red circles) projectiles for velocities above 1 a.u. For the TI channel, the cross sections for C^{3+} are a little larger than those for He^{2+} projectiles, both being still much larger than those for He^+.

These features can be better analyzed if one plots the ratio between the TI and the SC cross sections, σ_{TI}/σ_{SC}, as a function of the projectile charge state, q. This is shown in Fig. 5, where these ratios are represented for several collision systems at the fixed projectile velocity of 3.16 a.u., namely, H^+, He^{2+}, and Li^{3+} ions on He from Shah and Gilbody [57], He^+ on He from Forest *et al.* [58], He^+ and He^{2+} ions on He, Ne, Ar, and Kr from DuBois [62,63], and C^{3+} from the present work (He, Ar, Kr, and Xe targets) and from Kirchner *et al.* (Ne target) [10]. It can be readily seen that the ratios for the He target (green squares) follow approximately the q^2-scaling rule for $q \leqslant 3$ analyzed by Montenegro *et al.* [76] for a higher velocity (≈9 a.u.), represented by the solid green line in Fig. 5. However, the behavior of the heavier targets (Ne, purple circles; Ar, blue triangles; Kr, red stars; and Xe, black diamond) is very different than that of He: not only there is no apparent difference concerning their atomic number, lying somewhat scattered between the two dashed lines drawn in Fig. 5, but also the dependence of the TI-to-SC ratio with the

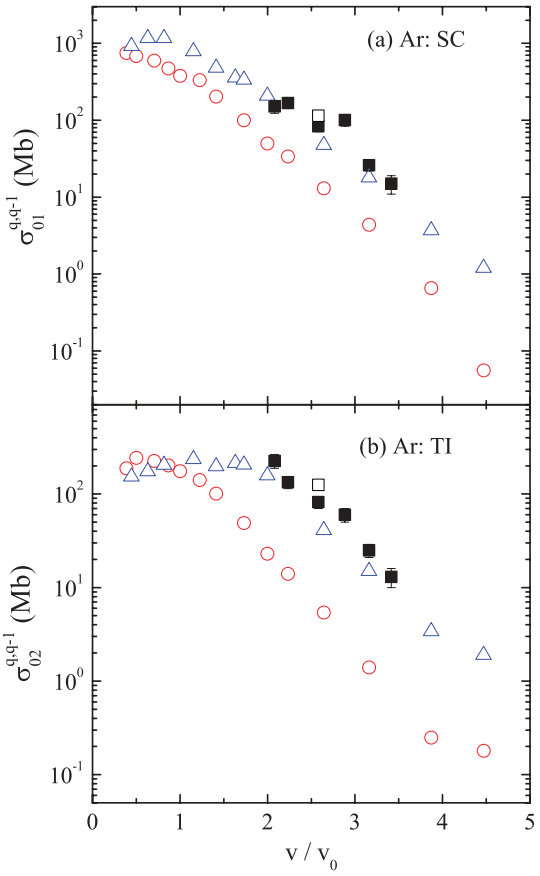

FIG. 3. (Color online) The same as in Fig. 2 for the Ar target. Symbols: black solid squares, C^{3+}, this work; black open squares, C^{3+}, from Ref. [66]; red circles, He^{+}, from Ref. [63]; and blue up triangles, He^{2+}, from Ref [62].

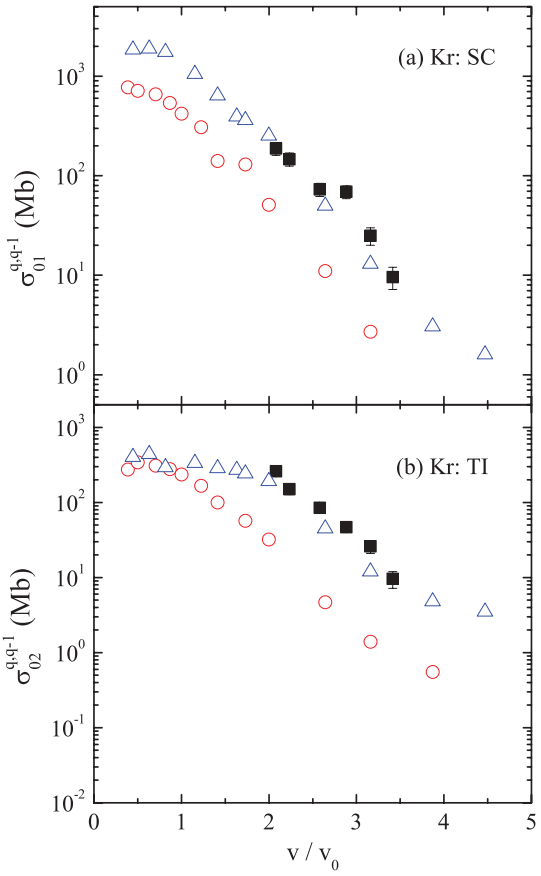

FIG. 4. (Color online) The same as in Fig. 3 for the Kr target. Symbols: black solid squares, C^{3+}, this work; red circles, He^{+}, from Ref. [63]; and blue up triangles, He^{2+}, from Ref [62].

projectile charge state tends to saturate as q increases. This fact, combined with the observations from Figs. 3 and 4, is probably due to an increase in the multiple-ionization processes which breaks down the simple q^2 law.

B. Single loss accompanied by target multiple ionization

The absolute cross sections for the multiple ionization of He, Ar, Kr, and Xe atoms accompanied by single-electron loss of the C^{3+} projectile, σ_{0j}^{34} with $j \neq 0$ [see Eq. (2)], are listed in Tables V to VIII as functions of the projectile energy.

It is well known that the electron loss of dressed projectiles is governed by two competing mechanisms, namely, the screening and antiscreening modes [33,77]. In the former, the projectile electron loss occurs due to the interaction between the active projectile electron ("active electron" meaning an electron which undergoes a transition during the collision, in the present case, a transition into the continuum) and the screened target nucleus; in this mechanism, the target electrons play a passive role of screening the target nuclear Coulomb field, and the target remains in its initial state; in this case, only the projectile electrons are active. In the latter mode, the projectile active electron interacts directly with the target electrons, usually resulting in the simultaneous ionization of both collision partners; thus, in the antiscreening mode, there are active electrons in both the projectile and the target [33,77].

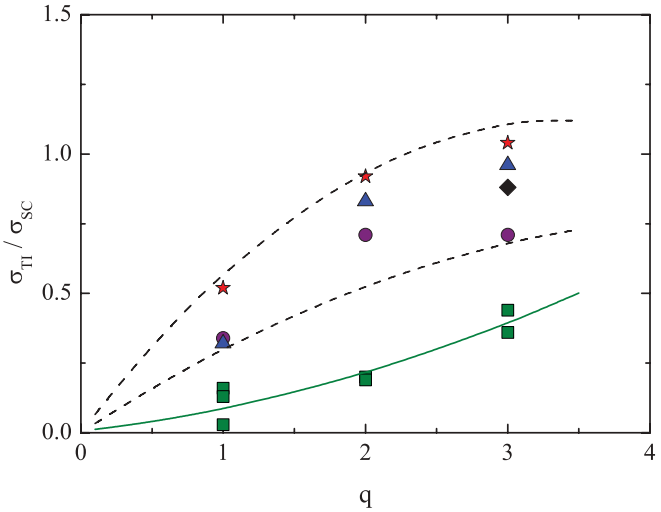

FIG. 5. (Color online) Ratio between σ_{TI} and σ_{SC}, as a function of the projectile charge state, q, for the collision velocity of 3.16 a.u. Targets: He, green squares; Ne, purple circles; Ar, blue triangles; Kr, red stars; and Xe, black diamond. Projectiles: C^{3+}, this work and Ref. [10]; H^{+}, He^{2+}, and Li^{3+}, from Ref. [57]; He^{+}, from Refs. [63] and [58]; and He^{2+}, from Ref [62]. Solid green line: q^2 fit to the ratios for the He target; black dashed lines, eye guides of the lower and upper limits to the ratios for the Ne, Ar, Kr, and Xe targets (see text).

TABLE V. Multiple-ionization absolute cross sections (in Mb) of He accompanied by single-electron loss of the C^{3+} projectile, as a function of the projectile energy, E.

E (MeV)	He^{+}	He^{2+}
2.0	3.1 ± 0.5	0.53 ± 0.10
2.5	5.3 ± 0.9	0.86 ± 0.15
3.0	5.7 ± 1.0	1.2 ± 0.2
3.5	4.5 ± 0.8	0.81 ± 0.15

In a recent article [73], the absolute total cross sections for the single-electron loss of B^{2+} and C^{3+} by Ne and Ar targets were measured. In that article, the authors presented a comparison of their experimental results with calculations of the total single-electron-loss cross sections as the sum of the two aforementioned mechanisms which contribute to the single-electron loss. In that work, the screening was calculated using the extended classical-impulse free-collision model as presented by Sigaud [40] and the PWBA, while the antiscreening was obtained from the PWBA extended sum-rule method of Montenegro and Meyerhof [70]. It was observed that the calculations using the free-collision model describe the experimental cross sections much better than the PWBA for both projectiles.

The same kind of comparison is presented here in Figs. 6–9. In these figures, the squares represent the sum of all single-loss–multiple-ionization cross sections measured here, called total loss-ionization cross section, $\sigma_{\text{inelastic}} = \sum_{j \neq 0} \sigma_{0j}^{34}$, while the triangles are the total electron-loss cross section from Ref. [8], σ_{loss}. The open circles represent the difference between the total electron-loss and total loss-ionization cross section and could be called "experimental screening," σ_{screen}, in the sense that this is the mode in which the target remains in its initial state. The solid lines are the sum of the screening contribution calculated using the extended free-collision model from Ref. [40] and the antiscreening contribution from Montenegro and Meyerhof [70], the dashed lines are the screening contribution from the extended free-collision model of Sigaud [40], the dotted lines are the sum of the screening and antiscreening contributions calculated within the PWBA [70], and the dash-dotted lines are the antiscreening contribution from Ref. [70]. It should be noted that the calculations for the screening using the free-collision model are limited to projectile velocities larger than the orbital velocity of the projectile active electron, which is 2.2 a.u. for C^{3+} projectiles [40]. Due to this constraint, the calculations performed with this model do not cover the whole region of velocities of the present measurements.

It should first be noted that, as also observed in Ref. [73], the overall agreement between the total single-electron-loss cross sections calculated using the free-collision model and the experimental total loss cross sections from Melo *et al.* [8] is very good for all the targets. Also, when one compares the calculations using this model with the "experimental screening" cross sections for the He target, the agreement is remarkably good. However, as the target atomic number increases, the agreement between theory and experiment becomes worse with increasing collision energy. In principle, this fact is quite unexpected, since the free-collision model should provide better results for increasing collision velocity [39,40]. However, the "experimental screening" cross sections have been obtained by subtracting the total loss-ionization cross section from total electron-loss cross sections. Thus, it has been assumed that the total loss-ionization cross sections presently measured, $\sigma_{\text{inelastic}}$, were due only to the electron-electron interaction, with no contribution coming from the direct interaction between the projectile (or target) electrons and the screened target (or projectile) nucleus. Actually, the importance of this process in comparison to the antiscreening has already been suggested by the calculations of Kirchner and co-workers [10] for the C^{3+}–Ne system in the same velocity range as the present data. It should also be mentioned that the fluctuations observed in the "experimental screening" cross sections, especially for the Kr target at $v = 3.16$ a.u., may be due to some fluctuations in the experimental electron-loss–multiple-ionization cross sections, which are amplified by the subtraction procedure.

In Ref. [73], the authors have tried to analyze the antiscreening contribution, although they had not measured this contribution separately, following the reasoning presented by Montenegro *et al.* [71] for the electron loss of He^{+} ions by noble gases, within the independent particle model (IPM). Here we have followed the same procedure as in [71] and have plotted in Fig. 10 the ratio between $\sigma_{\text{inelastic}}$ and the ionization cross sections of C^{3+} ions by electrons from Crandall *et al.* [78], σ_{e}, here called the "experimental ratio," as a function of the projectile energy. Also shown are the ratios between the PWBA-based calculations for the antiscreening contribution for the present collision systems from Montenegro and Meyerhof [70], σ_{anti}, and the calculations for the ionization cross sections of C^{3+} by electrons according to the fitting function presented by Mattioli *et al.* [79] based on the distorted-wave exchange model [80], here called the "theoretical ratio." The data from Kirchner *et al.* [10] for the Ne target are also included for completeness. In the case of the electron-impact data, the collision energies are those equivalent to the heavy-ion projectiles with the same velocity.

TABLE VI. Multiple-ionization absolute cross sections (in Mb) of Ar accompanied by single-electron loss of the C^{3+} projectile, as a function of the projectile energy, E.

E (MeV)	Ar^{+}	Ar^{2+}	Ar^{3+}	Ar^{4+}	Ar^{5+}	Ar^{6+}
2.0	10 ± 2	8.6 ± 1.5	5.5 ± 0.9	3.2 ± 0.6	1.1 ± 0.3	0.5 ± 0.13
2.5	13 ± 2	12 ± 2	9.9 ± 1.7	4.4 ± 0.8	1.7 ± 0.5	1.1 ± 0.3
3.0	28 ± 5	23 ± 4	11 ± 2	4.1 ± 0.8	1.4 ± 0.4	0.8 ± 0.2
3.5	29 ± 5	27 ± 5	10 ± 2	3.4 ± 0.6	2.4 ± 0.5	1.1 ± 0.3

TABLE VII. Multiple-ionization absolute cross sections (in Mb) of Kr accompanied by single-electron loss of the C^{3+} projectile, as a function of the projectile energy, E.

E (MeV)	Kr^{+}	Kr^{2+}	Kr^{3+}	Kr^{4+}	Kr^{5+}	Kr^{6+}	Kr^{7+}
2.0	6.5 ± 1.0	4.7 ± 0.8	4.1 ± 0.7	1.9 ± 0.4	1.5 ± 0.4	0.59 ± 0.2	0.51 ± 0.15
2.5	10 ± 2	10 ± 2	7.2 ± 1.3	3.8 ± 0.8	2.2 ± 0.6	1.5 ± 0.5	0.81 ± 0.25
3.0	30 ± 5	27 ± 5	15 ± 3	5.6 ± 1.1	3.5 ± 0.8	3.8 ± 0.8	1.3 ± 0.4
3.5	26 ± 4	22 ± 4	14 ± 3	5.9 ± 1.1	3.8 ± 0.8	3.8 ± 0.8	1.1 ± 0.3

A behavior for the experimental and theoretical ratios $\sigma_{\text{inelastic}}/\sigma_{\text{e}}$ and $\sigma_{\text{anti}}/\sigma_{\text{e}}$ similar to that of those found by Montenegro *et al.* [71] for He^{+} projectiles can also be observed here, with the theoretical ratios reaching a maximum for C^{3+} energies between 4 and 5 MeV, with a slow variation at higher energies, except for the He target, which presents no maximum and a slight monotonic decrease with increasing energy. The experimental ratios seem to follow approximately the trends of the theoretical ones, although the limited range of the present measurements does not allow a more conclusive analysis.

As mentioned previously, the antiscreening mode is due to the interaction between the projectile active electrons and the electrons in the target. It is clear, however, that not all of the target electrons contribute actively to the antiscreening cross sections on the same footing, mainly due to the differences between their binding energies [81]. Those which effectively contribute to the projectile electron loss in the antiscreening mode are called here "target active electrons." If one considers, then, that the ratio $\sigma_{\text{anti}}/\sigma_{e}$ provides an estimate of the average number of target active electrons, $\langle n_0 \rangle$, as in [71], one can see from Fig. 10 that $\langle n_0 \rangle$ depends on the collision energy. Thus, one can, for instance, write

$$\langle n_0 \rangle_E = f(E) \langle n_0 \rangle_a, \tag{6}$$

where $\langle n_0 \rangle_a$ is the value of the average number of target active electrons taken at the impinging energy of 100 MeV (for reasons to be discussed later), and $f(E)$ is some function of the collision energy, E.

Taking for $\langle n_0 \rangle_a$ the values obtained from Fig. 10 at 100 MeV, namely, 0.63 for He, 2.9 for Ne, 5.6 for Ar, 9.6 for Kr, and 14.1 for Xe, we have plotted in Fig. 11 the calculated values of $f(E)$ for the different targets (here represented by symbols to make clearer their behavior with the energy) as a function of the collision energy. All targets—with the exception of He—present the same behavior: a fast increase just above threshold, followed by a sharp maximum—which lies between 4 and 5 MeV for all targets—and a slow decrease with increasing energy; the He target presents no maximum, decreasing monotonically with the collision energy. The most notable feature is that the values of $f(E)$ coalesce along the same curve for all targets above the maximum region, including He. We have then tried to fit a simple curve, which could act as a "universal" function to estimate the average number of target electrons active for the antiscreening as a function of the collision energy for the C^{3+} projectile ion. The fitted function, shown in Fig. 11 as a solid black line, was

$$f(E) = 4.514 - \frac{3.831E}{9.707 + E}. \tag{7}$$

It should be emphasized here that the above function can be considered as a "universal" function with respect to the target for the specific case of the C^{3+} projectile. It has yet to be shown if this "universality" holds for the antiscreening contribution for the electron loss of other projectiles.

Thus, following the reasoning of Montenegro *et al.* [71] for the He^{+} projectile, one can plot the ratios between the experimental $\sigma_{\text{inelastic}}$ and $\langle n_0 \rangle_E$ and the ratio between the theoretical σ_{anti} and $\langle n_0 \rangle_E$ and compare them with the ionization cross sections of C^{3+} by electrons. This has been done in Fig. 12, where these ratios—calculated using the values of $\langle n_0 \rangle_E$ obtained using Eqs. (6) and (7)—are shown together with the experimental data for electron ionization of C^{3+} by electrons from Crandall *et al.* [78]. Again, a behavior similar to that seen for He^{+} projectiles from Ref. [71] has been observed. All theoretical ratios coalesce for energies above approximately 10 MeV (for He^{+} this occurred for $E > 3.0$ MeV) and agree very well with the electron ionization data for energies above the maximum. Below the maximum, the ratio $\sigma_{\text{anti}}/\langle n_0 \rangle_E$ for He (solid green line) provides the best description of the electron data.

In order to have an analytical estimate of the number of target active electrons, we have used the impulse approximation (IA) for the antiscreening from Montenegro and Zouros [81]. In this approximation, the antiscreening can be regarded, in the projectile frame, as the ionization of the projectile by a beam of $\langle n_0 \rangle$ target electrons [71,81]. In the intermediate-velocity

TABLE VIII. Multiple-ionization absolute cross sections (in Mb) of Xe accompanied by single-electron loss of the C^{3+} projectile, as a function of the projectile energy, E.

E (MeV)	Xe^{+}	Xe^{2+}	Xe^{3+}	Xe^{4+}	Xe^{5+}	Xe^{6+}	Xe^{7+}	Xe^{8+}	Xe^{9+}	Xe^{10+}	Xe^{11+}
2.0	14 ± 2	13 ± 2	9.0 ± 1.5	4.7 ± 0.8	3.4 ± 0.7	1.2 ± 0.3	0.9 ± 0.3				
2.5	20 ± 3	22 ± 4	13 ± 2	8.5 ± 1.5	6.3 ± 1.3	3.5 ± 0.9	3.4 ± 0.9				
3.0	22 ± 4	24 ± 4	13 ± 2	6.9 ± 1.2	6.6 ± 1.2	5.0 ± 1.3	3.2 ± 0.8	4.2 ± 1.3	2.5 ± 0.8	1.6 ± 0.5	0.5 ± 0.2
3.5	22 ± 4	21 ± 4	13 ± 2	9.2 ± 1.7	6.4 ± 1.3	5.7 ± 1.2	4.2 ± 0.9	3.4 ± 0.7	1.7 ± 0.5	1.6 ± 0.5	0.9 ± 0.3

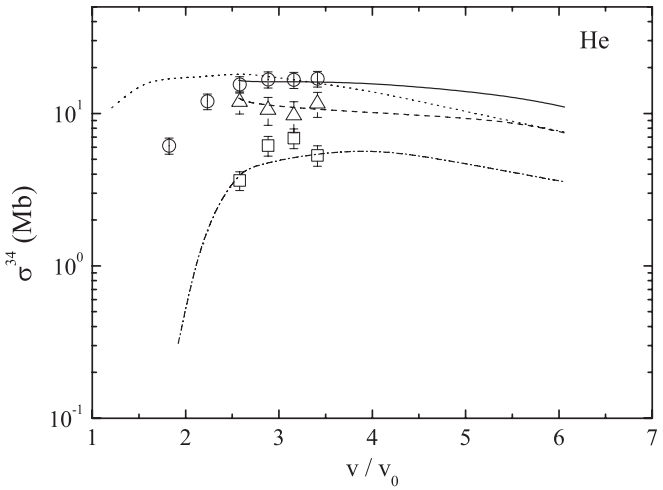

FIG. 6. Absolute single-electron-loss cross sections (in Mb) of C^{3+} by He as a function of the projectile velocity in atomic units. Experiment: squares, sum of all loss-ionization cross sections, this work; circles, total electron-loss cross section from Ref. [8], and triangles, difference between the total electron-loss and total loss-ionization cross section. Theory: solid line, sum of screening (extended free-collision model from Ref. [40]) and antiscreening (Ref. [70]); dashed line, screening (extended free-collision model from Ref. [40]); dotted line, sum of screening and antiscreening in the PWBA (Ref. [70]); dash-dotted line, antiscreening (Ref. [70]) (see text).

regime, the antiscreening cross section, in atomic units, can be written in the IA as [81]

$$\sigma_{\text{anti}}^{\text{IA}} = \int_{-\infty}^{+\infty} dv_z \sigma_{if}[q_{\min}(v_z)] J(v_z), \tag{8}$$

where

$$\sigma_{if}(q_{\min}) \approx \frac{8\pi}{V^2} \int_{q_{\min}}^{\infty} \frac{dq}{q^3} |F_{if}(q)|^2 \tag{9}$$

is the cross section for the ionization of the projectile in an initial state i (the final state f lying in the continuum) by a pointlike particle of unit charge calculated in the PWBA

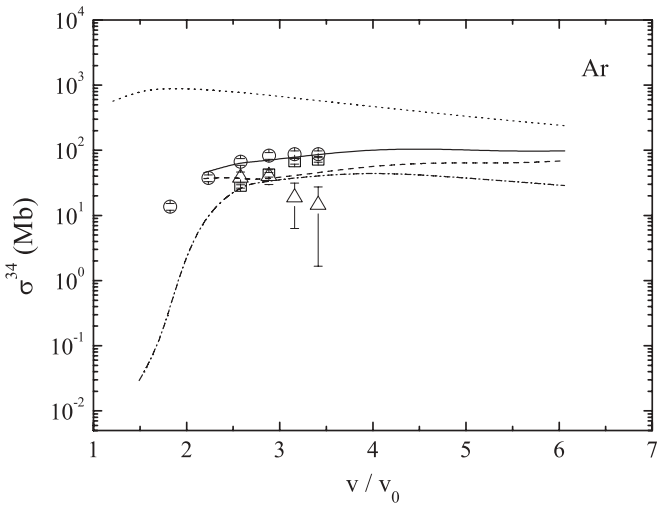

FIG. 7. The same as in Fig. 6 for the Ar target.

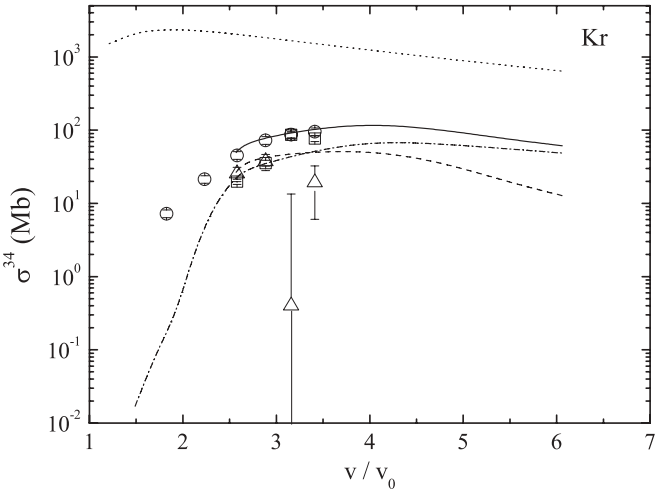

FIG. 8. The same as in Fig. 6 for the Kr target.

[82]. In Eqs. (8) and (9), $q_{\min}$ is the minimum momentum q transferred in the collision, given by [81]

$$q_{\min} \approx \frac{\Delta E_p + I_t}{V + v_z}, \tag{10}$$

$\vec{V} = V\hat{\mathbf{z}}$ is the collision velocity, $J(v)$ is the momentum distribution (Compton profile) of the target active electron in its initial state, v_z is the component along the beam direction of the peaking velocity of the Compton profile, $F_{if}(q) = \langle f|e^{-i\mathbf{q}\cdot\mathbf{r}}|i\rangle$ is the projectile transition amplitude, ΔE_p is the difference between the final, E_f, and initial, E_i, energies of the projectile active electron, and I_t is the ionization energy of the target active electron.

In the case where more than one target electron can actively contribute to the projectile electron loss in the antiscreening mode, if these potentially active electrons belong to different subshells of the target atom, then their ionization energies, I_t, have different values. Since, as shown in Eq. (10), $q_{\min}$ which appears in the integral of Eq. (9) depends on I_t, the contributions from the target subshells with different values of

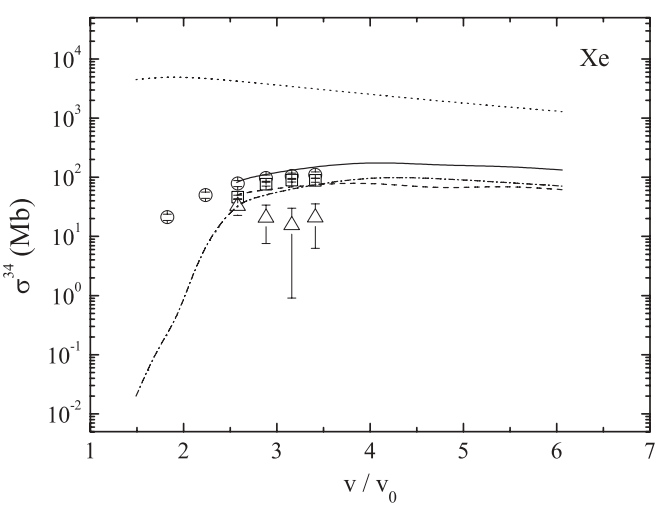

FIG. 9. The same as in Fig. 6 for the Xe target.

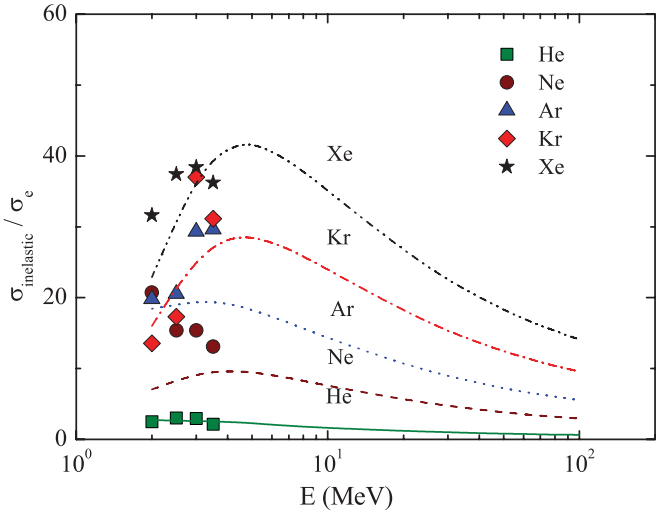

FIG. 10. (Color online) Ratios between the single-electron-loss cross sections for C^{3+} projectiles concomitantly with target multiple ionization ($\sigma_{\text{inelastic}}$) and the ionization of C^{3+} by electrons with the same velocity (σ_e) as a function of the collision energy. The symbols are the present measurements for He (green squares), Ar (blue triangles), Kr (red diamonds), and Xe (black stars), and Ne (purple circles) from Ref. [10]. The lines are the ratios of calculations for the antiscreening contribution from Ref. [70] and the ionization cross sections of C^{3+} ions by electron impact [79]: solid green line, He; dashed purple line, Ne; dotted blue line, Ar; dash-dotted red line, Kr; and dash-dot-dotted black line, Xe. The energies of the electron-impact data are those equivalent to the heavy-ion projectiles with the same velocity (see text).

I_t must be taken into account separately; thus, Eq. (10) can be written as

$$q_{\text{min}}^{nl} \approx \frac{\Delta E_p + I_{nl}}{V + v_z}, \tag{11}$$

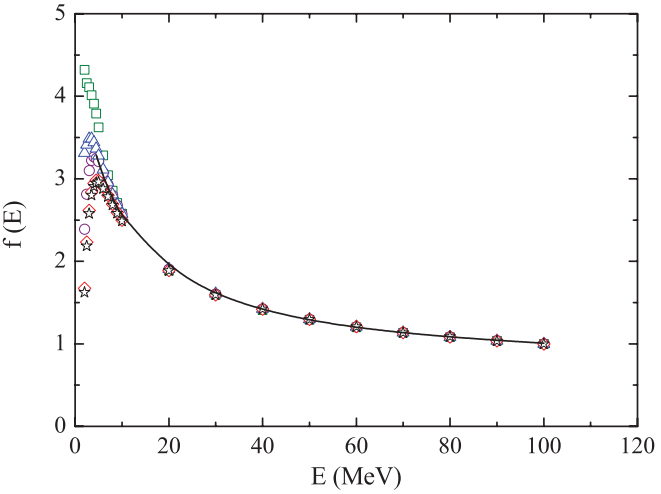

FIG. 11. (Color online) Ratios between $\langle n_0 \rangle_E$ and $\langle n_0 \rangle_a$ as a function of the collision energy. The symbols are the calculated values for He (green squares), Ne (purple circles), Ar (blue triangles), Kr (red diamonds), and Xe (black stars). The solid black line is the fitted function $f(E)$ (see text).

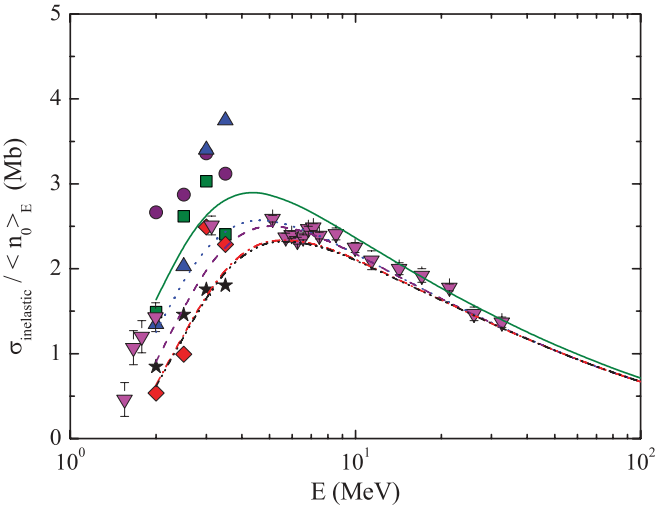

FIG. 12. (Color online) Ratios between $\sigma_{\text{inelastic}}$ and the average number of target active electrons for the antiscreening, $\langle n_0 \rangle_E$, obtained from Eqs. (6) and (7), for noble gas targets as a function of the collision energy. The symbols are the present measurements for He (green squares), Ar (blue up triangles), Kr (red diamonds), and Xe (black stars); Ne (purple circles) from Ref. [10]; and electrons (magenta down triangles) from Ref. [78]. Theory: PWBA-based calculations for the antiscreening contribution from Ref. [70]: solid green line, He; dashed purple line, Ne; dotted blue line, Ar; dash-dotted red line, Kr; and dash-dot-dotted black line, Xe. The energies of the electron-impact data are those equivalent to the heavy-ion projectiles with the same velocity (see text).

where q_{min}^{nl} is the minimum momentum transfer for an electron occupying the nl subshell of the target, with principal and orbital quantum numbers n and l, respectively, and I_{nl} is its ionization energy. Thus, Eq. (8) should be rewritten as

$$\sigma_{\text{anti}}^{\text{IA}} = \sum_{nl} \left(\sigma_{\text{anti}}^{\text{IA}}\right)_{nl}, \tag{12}$$

where

$$\left(\sigma_{\text{anti}}^{\text{IA}}\right)_{nl} = \int_{-\infty}^{+\infty} dv_z \sigma_{if}\left[q_{\text{min}}^{nl}(v_z)\right] J(v_z) \tag{13}$$

is the antiscreening cross section due to the interaction of the projectile electron with an electron occupying the nl subshell of the target atom.

Furthermore, in the high-energy limit, one can consider $v_z \ll V$, so that Eq. (11) becomes

$$q_{\text{min}}^{nl} \approx \frac{\Delta E_p + I_{nl}}{V}. \tag{14}$$

The consequence of this approximation is that $\sigma_{if}(q_{\text{min}}^{nl})$ does not depend on v_z any longer and can be taken out from the integral in Eq. (12), which can, then, be easily performed for each subshell nl, providing

$$\left(\sigma_{\text{anti}}^{\text{IA}}\right)_{nl} = N_{nl}\sigma_{if}\left(q_{\text{min}}^{nl}\right), \tag{15}$$

where N_{nl} is the number of electrons in subshell nl of the target atom. So, the cross section for the antiscreening in the IA can be written as

$$\sigma_{\text{anti}}^{\text{IA}} = \sum_{nl} N_{nl}\left(\sigma_{\text{anti}}^{\text{IA}}\right)_{nl}. \tag{16}$$

In the high-velocity regime, one can use the Bethe approximation to evaluate $\sigma_{if}(q_{\min})$ in terms of the collision velocity [83], thus finding

$$\sigma_{if}(q_{\min}) = \frac{1}{\left(1+\frac{I_{nl}}{\Delta E_p}\right)}\sigma_{if}\left(\frac{\Delta E_p}{V}\right), \tag{17}$$

so that Eq. (16) can be rewritten as

$$\sigma_{\text{anti}}^{\text{IA}} = \left[\sum_{nl}\frac{N_{nl}}{\left(1+\frac{I_{nl}}{\Delta E_p}\right)}\right]\sigma_{if}\left(\frac{\Delta E_p}{V}\right). \tag{18}$$

Defining

$$\langle n_0\rangle_{nl} = \frac{N_{nl}}{\left(1+\frac{I_{nl}}{\Delta E_p}\right)}, \tag{19}$$

as the average number of target electrons in a given subshell nl which contribute actively to the antiscreening, and

$$\langle n_0\rangle = \sum_{nl}\langle n_0\rangle_{nl} \tag{20}$$

as the total average number of target active electrons, one can finally write the IA antiscreening cross section from Eq. (18) as

$$\sigma_{\text{anti}}^{\text{IA}} = \langle n_0\rangle\sigma_{if}. \tag{21}$$

Thus, one can write the total average number of target active electrons as a sum of the contributions from all target subshells in the high-velocity regime. Using the ionization energies for the subshells of the noble gases from Ref. [84] in Eq. (19), we have found the following values for $\langle n_0\rangle$ using Eq. (20): 1.4 for He, 5.8 for Ne, 7.8 for Ar, 12.4 for Kr, and 15.1 for Xe, which are close to the values of $\langle n_0\rangle_a$ mentioned above, $\langle n_0\rangle_a$, obtained from the values of $\langle n_0\rangle$ at 100 MeV in the plots in Fig. 10. This can be seen in Fig. 13, where we have plotted the values of $\langle n_0\rangle$ as a function of the target atomic number, Z_{target}, obtained from Eq. (20) (triangles), together with those extracted from Fig. 10 at 4.0 MeV (squares) and 100 MeV (circles). It can be seen that the values obtained within the Bethe approximation agree quite well with the high-energy ones, derived from the PWBA-based calculations of the antiscreening of Montenegro and Meyerhof [70], showing that the approaches used here are consistent.

It should be emphasized that Eqs. (8) and (9) were obtained in Ref. [81] under the assumption that, for intermediate-velocity collisions, if $\Delta E_p \gg I_t$, then $q_{\min}$ is large when compared with the average momentum of the outer-shell target electrons. Since $q_{\min}$ is inversely proportional to the collision velocity, this condition is not satisfied for very high velocities and the results obtained here are no longer valid. On the other hand, $\langle n_0\rangle_E$, defined as the ratio $\sigma_{\text{anti}}/\sigma_e$ as a function of E, can only be interpreted within the impulse approximation—that is, in the projectile frame of reference, as the interaction of the projectile electron with a "beam" of target electrons—for high-velocity collisions. Thus, these assumptions imply a velocity range in which the present procedure can be used. For C^{3+} projectiles, this velocity range lies between approximately 10 and 20 a.u. This was the reason why we have chosen the values of $\langle n_0\rangle_a$ at the collision energy of 100 MeV ($V \simeq 18$ a.u.).

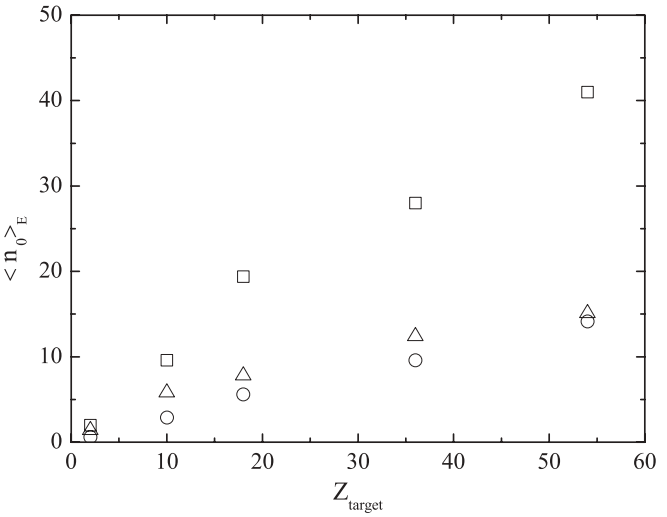

FIG. 13. Average number of target active electrons for the antiscreening, $\langle n_0\rangle$, as a function of the target atomic number. Symbols: values of $\langle n_0\rangle$ taken from Fig. 10 at collision energies of 4 MeV (squares) and 100 MeV (circles), while the triangles represent the values of $\langle n_0\rangle$ calculated using Eq. (21) (see text).

The procedure described previously allows one to estimate the partial contribution from each target subshell to the total number of active electrons, $\langle n_0\rangle_{nl}$. Figure 14 is a bar chart of the ratio between the number of active electrons in each subshell nl and the total number of electrons in the same subshell, $\langle n_0\rangle_{nl}/N_{nl}$, for the noble gases from He to Xe. As expected, the largest contributions come from the outer-shell electrons; nevertheless, it is interesting to notice that the relative fractions of active electrons for the outermost subshell do not vary much among the targets, lying approximately

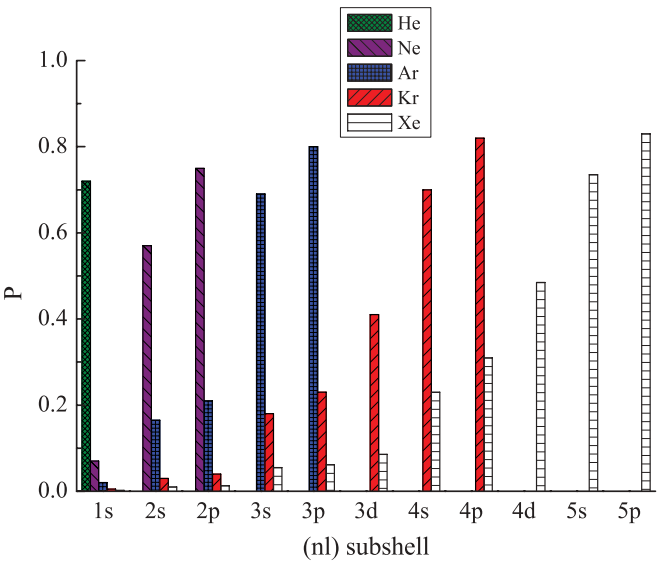

FIG. 14. (Color online) Number of active electrons for the antiscreening per each target-atom subshell nl, $\langle n_0\rangle_{nl}$, calculated according to Eq. (19) for noble gases from He to Xe, normalized to the total number of electrons in the nl subshell, N_{nl} (see text).

TABLE IX. Pure multiple-ionization absolute cross sections (in Mb) of He by C^{3+}, as a function of the projectile energy, E.

E (MeV)	He^+	He^{2+}
1.3	213 ± 32	26 ± 4
1.5	275 ± 43	25 ± 4
2.0	320 ± 48	30 ± 5
2.5	356 ± 53	36 ± 6
3.0	344 ± 52	36 ± 6
3.5	322 ± 48	33 ± 6

between 70% and 80% of the total number of electrons in that outermost subshell. However, it should be noted that this distribution may not be strictly true in the velocity range of the present measurements, since Eq. (19) is possibly not valid in this range, where the impulse approximation fails. As shown previously, the total average number of active target electrons is a velocity-dependent parameter and so should also be the contributions from the target subshells.

C. Pure multiple ionization

The absolute cross sections for the multiple ionization of He, Ar, Kr, and Xe atoms with the C^{3+} projectile remaining in its original charge state, σ_{0j}^{33} with $j \neq 0$ [see Eq. (3)], are listed in Tables IX to XII as functions of the projectile energy.

The largest cross sections are those for the pure single-ionization channel, σ_{01}^{33},

$$C^{3+} + T^0 \rightarrow C^{3+} + T^+, \tag{22}$$

and for the pure double-ionization channel, σ_{02}^{33},

$$C^{3+} + T^0 \rightarrow C^{3+} + T^{2+}, \tag{23}$$

where T represents a given target.

In an attempt to analyze the dependence of the pure multiple-ionization channel with both the projectile charge states and velocities, we have first considered the single and double ionization of He.

Thus, in Fig. 15 we present the single-ionization (σ_{01}^{qq}) and double-ionization (σ_{02}^{qq}) cross sections of He for equivelocity projectiles ($v/v_0 = 3.16$ a.u.) with different charge states from 0 to 3, namely, H^+ [57], He^0 [64], He^+ [13,58,64], He^{2+} [62], and Li^{3+} [57], and the present results for C^{3+}. A remarkable feature of the plotted data is that the cross sections for the single ionization for different projectiles with the same charge state are very close to each other, following approximately a quadratic dependence on the projectile charge state, q, as expected for low values of q from first-order models [53]. The fact that, for these intermediate-velocity collisions, the cross sections depend only on the charge state, irrespective of the electronic structure of the projectile itself, is an indication that the pure single ionization of He is essentially a large-impact-parameter process. For the double ionization, these similarities do not seem to occur, with the cross sections for the heavier projectiles lying consistently above those for lighter ones with the same charge state. Unfortunately, this analysis could not be extended to higher projectile charge states due to the paucity of absolute pure multiple-ionization cross sections at this intermediate velocity.

However, a further analysis of the similarities and differences observed in Fig. 15 in the single- and-double ionization cross sections of He could be made as a function of the projectile velocity. In Figs. 16 and 17 we have plotted, respectively, the pure single- and double-ionization cross sections of He by several triply charged projectiles as a function of the collision velocity. Projectiles include C^{3+} (present data and from Knudsen *et al.* [56]), Li^{3+} (from Knudsen *et al.* [56], Shah and Gilbody [57], and Woitke *et al.* [65]), and B^{3+} (from Knudsen *et al.* [56]). The different behaviors of the single- and double-ionization cross sections can be immediately seen. All single-ionization cross sections for the various projectiles coalesce along the same curve, without any indication of predominance of any projectile. However, for the double ionization it can be observed that the cross sections for C^{3+} lie above those for the other projectiles. Nevertheless, a comment must be made at this point concerning the data for C^{3+} of Knudsen *et al.* [56], represented by stars in both Figs. 16 and 17. Except for the lower velocity point reported by these authors, the other data—which extend to velocities higher than the present ones—tend to coalesce with ours. Knudsen *et al.* [56] mention in their work that they have only considered the electron-capture channel in the low-energy data for projectiles with charge states 4 and 5, assuming that electron capture was negligible for low-velocity projectiles with lower charge states. However, at their lower velocity (around 2.3 a.u.), the SC cross section for C^{3+} on He is ~50% of the pure single-ionization one, while the TI cross section is twice as large as the pure double-ionization one. This can explain the discrepancy between our data and the lowest-energy points of Knudsen *et al.* [56]. Actually, if one crudely subtracts the values of our measured capture cross

TABLE X. Pure multiple-ionization absolute cross sections (in Mb) of Ar by C^{3+}, as a function of the projectile energy, E. Numbers in parentheses represent powers of 10.

E (MeV)	Ar^+	Ar^{2+}	Ar^{3+}	Ar^{4+}	Ar^{5+}	Ar^{6+}
1.3	4.83(2) ± 0.66(2)	1.59(2) ± 2.3(1)	6.6(1) ± 0.9(1)	2.7(1) ± 0.4(1)	5.8(0) ± 1.2(0)	1.6(0) ± 0.4(0)
1.5	6.16(2) ± 0.92(2)	1.75(2) ± 2.6(1)	6.1(1) ± 0.9(1)	2.7(1) ± 0.5(1)	7.2(0) ± 1.5(0)	1.6(0) ± 0.4(0)
2.0	6.82(2) ± 1.02(2)	2.12(2) ± 3.2(1)	6.7(1) ± 1.0(1)	2.1(1) ± 0.4(1)	1.0(1) ± 2.0(0)	2.9(0) ± 0.7(0)
2.5	7.97(2) ± 1.20(2)	2.80(2) ± 5.2(1)	9.0(1) ± 1.1(1)	3.0(1) ± 0.6(1)	9.3(0) ± 2.4(0)	4.8(0) ± 1.4(0)
3.0	7.91(2) ± 1.19(2)	2.08(2) ± 4.0(1)	4.9(1) ± 0.7(1)	1.7(1) ± 0.3(1)	9.4(0) ± 1.1(0)	7.0(0) ± 2.1(0)
3.5	7.32(2) ± 1.10(2)	1.82(2) ± 2.9(1)	4.0(1) ± 0.7(1)	8.5(0) ± 1.7(0)	3.6(0) ± 1.1(0)	2.9(0) ± 0.6(0)

TABLE XI. Pure multiple-ionization absolute cross sections (in Mb) of Kr by C^{3+}, as a function of the projectile energy, E. Numbers in parentheses represent powers of 10.

E (MeV)	Kr^{+}	Kr^{2+}	Kr^{3+}	Kr^{4+}	Kr^{5+}	Kr^{6+}
1.3	5.39(2) ± 0.81(2)	1.98(2) ± 3.0(1)	9.5(1) ± 1.6(1)	3.1(1) ± 0.6(1)	1.4(1) ± 0.3(1)	5.3(0) ± 1.3(0)
1.5	7.49(2) ± 1.12(2)	2.46(2) ± 3.7(1)	1.04(2) ± 1.8(1)	3.5(1) ± 0.7(1)	1.5(1) ± 0.4(1)	7.7(0) ± 1.9(0)
2.0	7.72(2) ± 1.16(2)	2.71(2) ± 4.1(1)	1.18(2) ± 2.0(1)	3.5(1) ± 0.7(1)	1.9(1) ± 0.5(1)	9.8(0) ± 2.4(0)
2.5	9.05(2) ± 1.35(2)	2.63(2) ± 3.9(1)	1.03(2) ± 1.8(1)	3.2(1) ± 0.6(1)	2.0(1) ± 0.5(1)	1.8(1) ± 5.0(0)
3.0	8.53(2) ± 1.28(2)	2.39(2) ± 3.8(1)	9.1(1) ± 1.7(1)	2.7(1) ± 0.6(1)	1.7(1) ± 0.5(1)	1.7(1) ± 5.0(0)
3.5	7.92(2) ± 1.19(2)	2.03(2) ± 3.2(1)	8.4(1) ± 1.5(1)	1.7(1) ± 0.5(1)	1.2(1) ± 0.2(1)	8.1(0) ± 2.7(0)

sections from their low-velocity single- and double-ionization data one obtains values which are quite compatible with the present data.

We have also investigated the validity of the q^2 dependence of the pure single-ionization cross sections—predicted by first-order theories [53]—for the targets considered here as a function of the collision velocity, for different projectiles with charge states up to 8, in the intermediate- to high-velocity region. In Fig. 18, we present the ratios σ_{01}^{qq}/q^2 for He, while in Fig. 19 the same ratios for Ar, Kr, and Xe are shown, as functions of the projectile velocity. It should be mentioned that the recommended values for the ionization cross sections by H^+ projectiles from Ref. [85], plotted as red diamonds in Fig. 19, refer to total inclusive ionization cross sections; the inclusion of these data in Fig. 19 can be justified because, for H^+ projectiles, the single ionization is much larger than the other multiple-ionization channels. It can be readily noted that, although the ratios σ_{01}^{qq}/q^2 present similar behaviors with the collision velocity for all targets, they only coalesce for high velocities; the velocities above which the data for $q \geqslant 2$ join the ratios for $q = 1$ increase with the projectile charge state. This is more easily seen for the heavier targets: the data for He^{2+} for Ar and Kr (blue stars), for instance, are close to those for H^+ (red triangles and diamonds) and He^+ (red circles) for $v \approx 3$ a.u., while the corresponding velocity for C^{3+} (black squares) seems to be at a much larger value than the ones considered in the present work. For lower velocities, the ratios for the various charge states are rather different, for all targets, following a sequence with the charge state: the larger the values of q, the lower the ratio σ_{01}^{qq}/q^2. Although not shown in Fig. 19, the data from Tonuma *et al.* [67] for 1.05-MeV Ar^{q+} ions on Ar, with $q = 4$–14, show the same behavior.

Since Ar, Kr, and Xe are multielectronic targets, we have analyzed the q^2 dependence of the inclusive pure total-ionization cross sections, employing the inversion relations derived by Sant'Anna *et al.* [21] using the multinomial distribution within the IPM.

In brief, within the IPM, and considering only ionization and capture cross sections (since they are much larger than the electron-loss cross sections in the present case), the exclusive cross section for ionizing exactly one target electron without capturing any target electron (single ionization) is given by [21]

$$\sigma_{\rm ion} = N \int P_I(b)[1 - P_I(b) - P_C(b)]^{N-1} 2\pi b db, \quad (24)$$

where N is the total number of target electrons, and $P_I(b)$ and $P_C(b)$ are, respectively, the ionization and capture probabilities as functions of the impact parameter, b.

The integral in this equation couples $P_I(b)$ and $P_C(b)$. Since these probabilities depend differently on the projectile charge state, $\sigma_{\rm ion}$ is not expected to present a simple q dependence, unless the collision velocity is high enough so that one can consider $[1 - P_I(b) - P_C(b)] \simeq 1$.

On the other hand, following the notation of Ref. [21], the inclusive cross section for ionizing at least one target electron and capturing any number of electrons is given by

$$s_{\rm ion} = N \int P_I(b) 2\pi b db, \quad (25)$$

It should be stressed that Eq. (25) is not a high-velocity approximation. It is valid even at low velocities and small impact parameters, for which $P_I(b) + P_C(b) \simeq 1$. Thus, for low-to-intermediate velocities, a plot of $s_{\rm ion}$ is clearly more appropriate than a plot of $\sigma_{\rm ion}$ when looking for a simple q dependence of charge-changing cross sections.

While the measured cross sections in coincidence experiments are the exclusive ones, Sant'Anna *et al.* [21] have shown that it is possible to obtain experimental values for the inclusive cross sections from all measured exclusive cross sections from

TABLE XII. Pure multiple-ionization absolute cross sections (in Mb) of Xe by C^{3+}, as a function of the projectile energy, E. Numbers in parentheses represent powers of 10.

E (MeV)	Xe^{+}	Xe^{2+}	Xe^{3+}	Xe^{4+}	Xe^{5+}	Xe^{6+}
1.3	6.67(2) ± 1.00(2)	2.51(2) ± 4.0(1)	1.03(2) ± 1.8(1)	3.5(1) ± 0.6(1)	2.0(1) ± 3.0(0)	1.0(1) ± 2.0(0)
1.5	9.99(2) ± 1.50(2)	3.79(2) ± 5.7(1)	1.27(2) ± 2.0(1)	4.2(1) ± 0.8(1)	2.3(1) ± 5.0(0)	1.1(1) ± 3.0(0)
2.0	1.04(3) ± 1.55(2)	3.93(2) ± 5.9(1)	1.30(2) ± 2.2(1)	4.5(1) ± 0.8(1)	2.2(1) ± 4.0(0)	1.3(1) ± 3.0(0)
2.5	1.15(3) ± 1.72(2)	3.50(2) ± 5.6(1)	1.67(2) ± 2.8(1)	6.1(1) ± 1.2(1)	3.8(1) ± 8.0(0)	2.4(1) ± 5.0(0)
3.0	1.03(3) ± 1.54(2)	4.27(2) ± 6.8(1)	1.46(2) ± 2.5(1)	7.6(1) ± 1.5(1)	4.3(1) ± 9.0(0)	2.7(1) ± 6.0(0)
3.5	9.83(2) ± 1.47(2)	4.06(2) ± 6.5(1)	1.37(2) ± 2.3(1)	7.8(1) ± 1.6(1)	4.3(1) ± 9.0(0)	3.3(1) ± 7.0(0)

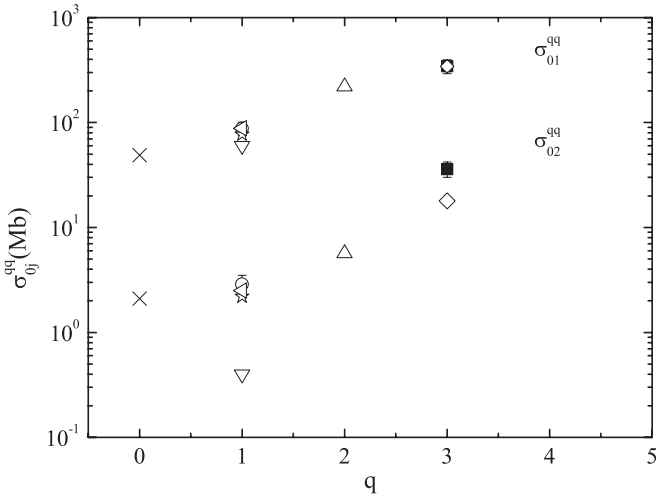

FIG. 15. Single- and double-ionization cross sections of He as a function of the projectile charge state, q, for the collision velocity of 3.16 a.u. C^{3+}: solid squares, this work; He^0: crosses, DuBois and Toburen [64]; H^+: inverted triangles, Shah and Gilbody [57]; He^+: circles, Santos *et al.* [13]; left triangles, DuBois and Toburen [64]; and stars, Forest *et al.* [58]; He^{2+}: up triangles, DuBois [62]; Li^{3+}: diamonds, Shah and Gilbody [57].

a charge-state coincidence experiment (and not only single ionization) through appropriate weighted sums.

In the case of interest of the present work, the transformation relation to obtain the inclusive cross section for the ionization of at least one target electron from our measured exclusive pure-ionization and electron-capture cross sections can be written as [21]

$$s_{ion} = \sum_{i=1}^{N} \sum_{j=0}^{N-j} (i-j)\sigma_{0i}^{q,q-j}. \tag{26}$$

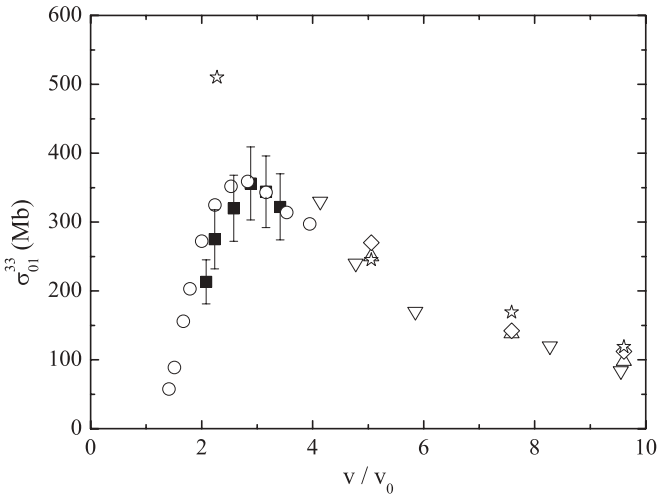

FIG. 16. Pure single-ionization cross sections of He by triply charged projectiles as a function of the projectile velocity in atomic units. C^{3+}: solid squares, this work; stars, Knudsen *et al.* [56]; Li^{3+}: circles, Shah and Gilbody [57]; up triangles, Knudsen *et al.* [56]; and down triangles, Woitke *et al.* [65]; B^{3+}: diamonds, Knudsen *et al.* [56].

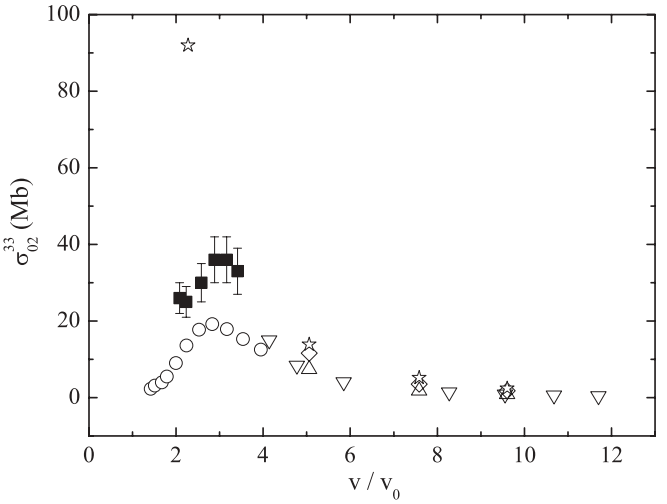

FIG. 17. The same as in Fig. 16 for the pure double ionization of He.

where j is the number of captured electrons and i is the number of electrons removed from the target. Therefore, $i - j$ is the number of ionized target electrons which are not captured by the projectile. In order to obtain numerical values, we truncate the series neglecting multiple capture (double, triple, and so on), which have not been measured in the present work, to obtain

$$s_{ion} = \sum_{i} \left[i\sigma_{0i}^{qq} + (i-1)\sigma_{0i}^{q,q-1} \right]. \tag{27}$$

The results for s_{ion}, obtained according to Eq. (27), divided by q^2, are plotted in Fig. 20, for the same collision systems as in Fig. 19, as functions of the projectile velocity. Although the ratios present a behavior similar to that of those for the pure single ionization for all targets, at low velocities they lie

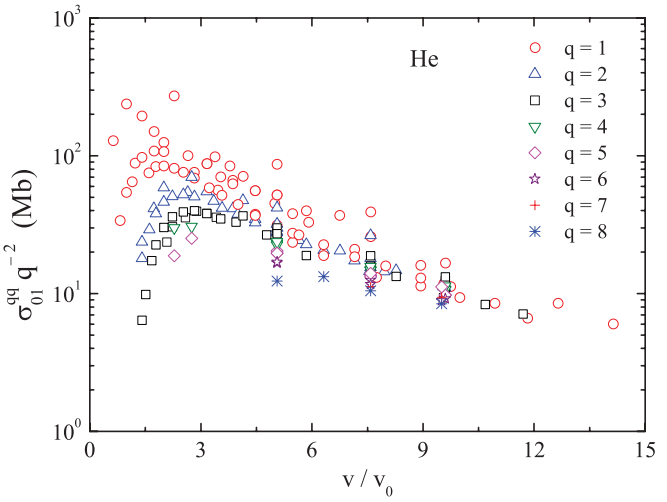

FIG. 18. (Color online) Ratios σ_{01}^{qq}/q^2 for the He target as a function of the projectile velocity in atomic units. Red circles, $q = 1$ from Refs. [13,26,52,56,57,63,65]; blue up triangles, $q = 2$ from Refs. [56,57,62,65]; black squares, $q = 3$, this work and from Refs. [56,57,65]; green down triangles, $q = 4$; magenta diamonds, $q = 5$; purple stars, $q = 6$; red crosses, $q = 7$; and blue asterisks, $q = 8$, all from Ref. [56].

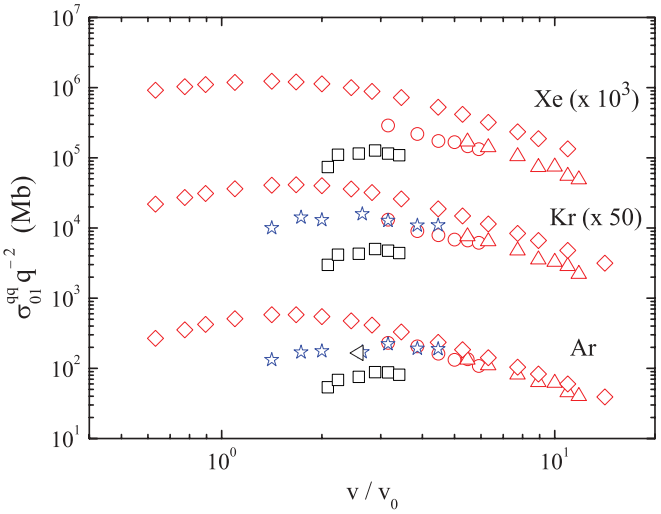

FIG. 19. (Color online) The same as in Fig. 18 for Ar, Kr, and Xe. Symbols: black squares, C^{3+}, this work; red circles, He^{+}, Ref. [13]; red up triangles, H^{+}, Ref. [26]; red diamonds, H^{+}, Ref. [85]; black left triangle, C^{3+}, Ref. [66]; and blue stars, He^{2+}, Ref. [62]. The ratios for Kr and Xe have been multiplied for 50 and 1000, respectively, in order to accommodate all data in the same figure.

much closer than those in Fig. 19. For example, at a velocity of 2.0 a.u., the ratio s_{ion}/q^2 for H^{+} is 60% larger than that for He^{2+}, in contrast to a factor of 3 observed for the same ratio in the single ionization for both Ar and Kr targets. The differences between the ratios s_{ion}/q^2 of the inclusive pure total-ionization and pure single-ionization cross sections for H^{+} and C^{3+} are even larger: for all targets, at 2.0 a.u., these ratios for H^{+} are 3 times larger than those for C^{3+} for the inclusive total-ionization cross sections, while they can be up to 15 times larger in the single-ionization case.

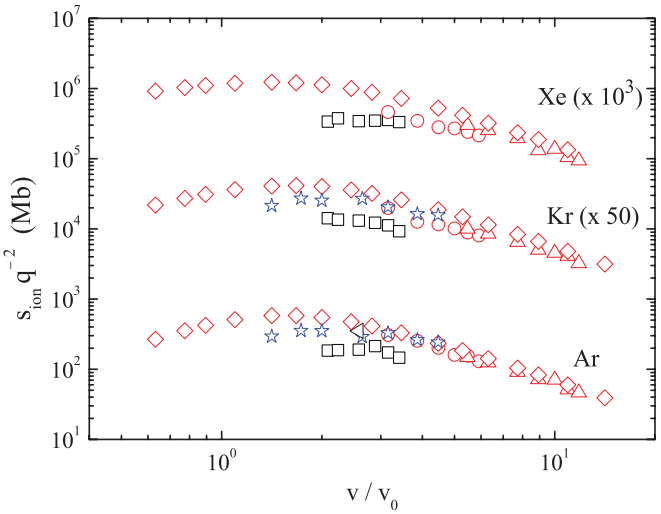

FIG. 20. (Color online) Ratios s_{ion}/q^2 for Ar, Kr, and Xe as a function of the projectile velocity in atomic units, with s_{ion} calculated according to Eq. (27). Symbols: black squares, C^{3+}, this work; red circles, He^{+}, Ref. [13]; red up triangles, H^{+}, Ref. [26]; red diamonds, H^{+}, Ref. [85]; black left triangle, C^{3+}, Ref. [66]; and blue stars, He^{2+}, Ref. [62]. The ratios for Kr and Xe have been multiplied by 50 and 1000, respectively, in order to accommodate all data in the same figure.

Another remarkable feature is that the ratios σ_{01}^{qq}/q^2 for the same value of q are very similar, irrespective of the projectile, as can again be better observed from the data for the He target: for example, the data for $q = 3$ (represented by the black squares in Fig. 18) follow the same curve, although they come from projectiles as different as Li^{3+}, B^{3+}, and C^{3+}. For the heavier targets, the only available data for different projectiles with the same charge states are for $q = 1$ (red diamonds, circles, and triangles); for those, the same behavior is observed. The fact that the pure single-ionization cross section depends only on the charge state of the projectile, be it bare or dressed, is quite unexpected, because it indicates that, for this process, the electronic structure of the projectile is irrelevant, with a full nuclear screening by the projectile electrons. The projectile acts as a point charge and the expected additional decrease of the nuclear screening associated to close collisions is not observed.

IV. SUMMARY AND CONCLUSIONS

We have performed a comprehensive set of measurements of the absolute cross sections for the multiple ionization of He, Ar, Kr, and Xe targets by C^{3+} ions, in the energy range from 1.3 to 3.5 MeV, in which the channels of pure target multiple ionization, the single loss and the single capture, both accompanied by target multiple ionization, have been determined. The data obtained here were compared with the other available absolute experimental results, most of these referring to the He target.

In the case of the single capture accompanied by target multiple ionization, σ_{0j}^{32}, the comparison between the sum of all partial cross sections and the total single-capture cross sections from Melo *et al.* [8] and Wolff *et al.* [73] showed a very good agreement for all targets. It has also been observed that the total single-capture cross sections for heavy targets present no dependence with the target atomic number, lying systematically above those for the He target. Since all noble gases, except He, have the same outermost-shell configuration (ns^2np^6), this fact indicates that the total single-electron-capture cross section is not strongly dependent on the structures of the radial wave functions of the outermost electrons. Calculations using the simple semiclassical Bohr-Lindhard model as presented by Knudsen *et al.* [56], although not describing this latter observation, still can provide reasonable estimates for the single-electron capture in the intermediate-velocity regime.

We have analyzed the dependence of the SC and TI processes of the present targets on the projectile charge state, for various projectiles with different charge states. On the one hand, for low- to intermediate-velocity collisions, the He SC data for projectiles with the same charge state tend to coalesce as, for example, in the case of the C^{3+} and Li^{3+} projectiles, which are practically the same in the velocity region where they overlap. As the collision velocity increases, the data for He^{+} and Li^{+} projectiles tend to be larger than those for protons, a feature which also occurs for the TI channel. These observations indicate that, for the single capture from He, C^{3+} and Li^{3+} ions act as if they were structureless point charges,

a behavior which seems to be followed by doubly charged projectiles, at least at low velocities, but not by singly charged ones. On the other hand, for the heavier targets, Ar and Kr, it has been observed that the behaviors of the cross sections are very similar to each other, being quite different than for the He target. For both SC and TI channels, the data for the C^{3+} and He^{2+} projectiles are very close, being much larger than those for the He^{+} projectiles.

We have also investigated the ratio between the TI and the SC cross sections as a function of the projectile charge state, q, at a fixed projectile velocity of 3.16 a.u. We have observed that the ratios for the He target follow approximately the q^2-scaling rule for $q \leqslant 3$, in agreement with the results of Montenegro *et al.* [76] for a higher velocity. However, the behavior for the heavier targets is very different than that of He: not only there is no apparent difference concerning their atomic number but also the dependence of the TI-to-SC ratio on the projectile charge state tends to saturate as q increases.

For the channel of single loss accompanied by target multiple ionization, we have compared our results to theoretical calculations in the PWBA [70] and the extended free-collision model [40] for the screening contribution, while the anticreening contribution has been evaluated using the PWBA extended sum-rule method of Montenegro and Meyerhof [70]. The overall agreement between the total single-electron-loss cross sections calculated using the free-collision model and the experimental total-loss cross sections from Melo *et al.* [8] is very good for all targets. Also, when one compares the calculations using the free-collision model with the "experimental screening," obtained by subtracting the sum of all cross sections for single loss accompanied by target multiple ionization from the total loss from Melo *et al.* [8], the agreement is remarkably good for the He target, getting worse with increasing collision energy for heavier targets. This has been attributed to the assumption that the total loss-ionization cross sections presently measured were due only to the electron-electron interaction, without considering the contributions from the direct interaction between the projectile (or target) electrons and the screened target (or projectile) nucleus.

We have analyzed the present calculations for the antiscreening contribution following the procedure presented by Montenegro *et al.* [71] for the electron loss of He^{+} ions by noble gases, within the independent particle model, and have found a similar behavior for C^{3+}. From this analysis, we have concluded that the average number of target electrons active in the antiscreening could be estimated from the ratios between the calculated antiscreening cross sections and the ionization of C^{3+} ions by electrons, being a function of the collision energy. Thus, we have been able to write this average number of target active electrons as the product of a rather simple universal function of the energy and the value of the average number of target active electrons in the high-velocity region. It is still to be verified whether this behavior also holds for other projectiles. We have also derived a simple method to estimate these numbers within the high-velocity Bethe approximation; the values obtained with this method agree quite well with the high-velocity ones. With this method, we have been able to estimate the contribution from each target subshell to the total number of target active electrons, finding that, as expected, the dominant contribution comes from the outermost subshells of each target.

Finally, for the pure multiple-ionization channels, we have observed, for the fixed velocity of 3.16 a.u., that the single-ionization cross sections of the He target are almost equal for projectiles with the same charge state, irrespective of their atomic number, thus presenting the same point-charge behavior of the SC channel. This does not happen, however, for the pure double-ionization cross sections, which seem to depend on the atomic number of equally charged projectiles. When one considers only triply charged projectiles, the single- and double-ionization cross sections again present different behavior: in the former the data for all projectiles coalesce along the same curve, while in the latter, the cross sections for C^{3+} are consistently above those for the other projectiles. This point-charge behavior of the pure single-ionization cross section seems to hold for the He target for various projectiles with different charge states for velocities up to 15 a.u. For Ar, Kr, and Xe targets, the available data shows that it seems to be valid at least for singly charged projectiles. This result is quite surprising, because one would expect that dressed projectiles with a given charge state q would present an effective charge larger than q, due to the partial screening of the projectile electrons on the nucleus at the most likely impact parameters, thus increasing the ionization cross sections when compared to those for bare projectiles.

The analysis of the q^2 dependence of the pure single-ionization cross sections predicted by first-order models, for projectiles with charge states ranging from 1 up to 8, has indicated that it is only valid for the high-velocity regime for all the targets considered in the present work. At lower velocities, the ratios for projectiles with $q \geqslant 2$ lie below those for $q = 1$. The velocities with which the data tend to coalesce with those for the singly charged projectiles increase with the projectile charge state, as also do the differences between the ratios σ_{01}^{qq}/q^2 and those for $q = 1$. The differences seem to be more evident for the heavier targets than for He, but they can be clearly observed in the latter case, where the plethora of existent data allowed us to consider a large range of projectile charge states. For the heavier targets, the ratios s_{ion}/q^2, where s_{ion} are the inclusive pure total-ionization cross sections, calculated following the procedure introduced by Sant'Anna *et al.* [21], also showed a behavior similar to that of the pure single-ionization ones, although the results for multiply charged projectiles lie much closer to those for singly charged projectiles than in the case of single ionization. This has been attributed to the increase of the importance of the electron-capture channel with the projectile charge state as the collision velocity decreases.

Although the extensive analyses of the data presented in this work have been made separately for each collision channel, it seems clear that all these processes are deeply connected among themselves, so that one cannot properly analyze in detail any of them without considering the others, even in the simplest case, the He target.

ACKNOWLEDGMENTS

This work was supported in part by the Brazilian agencies CNPq, FINEP, CAPES, FAPERJ, and MCT(PRONEX).

TABLE XIII. List of the cross sections mentioned in the text.

Symbol	Denomination	Equation or reference
$\sigma_{0j}^{q,q-1}$	Target multiple ionization accompanied by projectile single-electron-capture cross section	Eq. (1)
$\sigma_{0j}^{q,q+1}$	Target multiple ionization accompanied by projectile single-electron-loss cross section	Eq. (2)
σ_{0j}^{qq}	Pure multiple-ionization cross section	Eq. (3)
$\sigma_{01}^{q,q-1}$	Pure single-electron-capture cross section (SC)	Eq. (4)
$\sigma_{02}^{q,q-1}$	Transfer-ionization cross section (TI)	Eq. (5)
$\sigma^{q,q-1}$	Total electron-capture cross section	$\sigma^{q,q-1} = \sum_{j\neq 0} \sigma_{0j}^{q,q-1}$
$\sigma_{\text{inelastic}}$	Total experimental loss-ionization cross section	$\sigma_{\text{inelastic}} = \sum_{j\neq 0} \sigma_{0j}^{q,q+1}$
σ_{loss}	Total experimental electron-loss cross section	Ref. [8]
σ_{screen}	"Experimental screening" cross section	$\sigma_{\text{screen}} = \sigma_{\text{loss}} - \sigma_{\text{inelastic}}$
σ_{anti}	Theoretical antiscreening cross section	Ref. [70]
σ_{e}	Electron-impact ionization cross section	Refs. [78] (expt.) and [79] (th.)
σ_{01}^{qq}	Pure single-ionization cross section	Eq. (22)
σ_{02}^{qq}	Pure double-ionization cross section	Eq. (23)
σ_{ion}	Exclusive single-ionization cross section	Eq. (24)
s_{ion}	Inclusive ionization cross section	Eqs. (25)–(27)

APPENDIX: DEFINITIONS OF THE CROSS SECTIONS

In Table XIII we present a summary of all the cross sections referred to in the text, in order of appearance. The first column of Table XIII lists the symbols used in the text for the cross sections, while the second column provides the denominations that have been given to them here. The last column of Table XIII contains either the equations in the present text or the references where the cross sections have been defined.

[1] J. S. Yoon and Y. D. Jung, Phys. Plasmas **6**, 3391 (1999).
[2] A. K. Kaminskii and A. A. Vasilev, Phys. Part. Nucl. **29**, 201 (1998).
[3] W. H. Liu and D. R. Schultz, Astrophys. J. **530**, 500 (2000).
[4] P. Wu, K. L. Heng, S. W. Yang, Y. F. Chen, R. S. Mohan, and P. H. C. Lim, Artif. Intell. Med. **1620**, 372 (1999).
[5] G. de M. Azevedo, P. L. Grande, M. Behar, J. F. Dias, and G. Schiwietz, Phys. Rev. Lett. **86**, 1482 (2001).
[6] R. D. DuBois *et al.*, Phys. Rev. A **68**, 042701 (2003).
[7] R. D. DuBois *et al.*, Phys. Rev. A **70**, 032712 (2004).
[8] W. S. Melo, M. M. Sant'Anna, A. C. F. Santos, G. M. Sigaud, and E. C. Montenegro, Phys. Rev. A **60**, 1124 (1999).
[9] T. Kirchner, M. Horbatsch, and H. J. Lüdde, J. Phys. B **37**, 2379 (2004).
[10] T. Kirchner, A. C. F. Santos, H. Luna, M. M. Sant'Anna, W. S. Melo, G. M. Sigaud, and E. C. Montenegro, Phys. Rev. A **72**, 012707 (2005).
[11] J. H. McGuire, Phys. Rev. Lett. **49**, 1153 (1982).
[12] A. C. F. Santos, A. Hasan, and R. D. DuBois, Phys. Rev. A **71**, 034701 (2005).
[13] A. C. F. Santos, W. S. Melo, M. M. Sant'Anna, G. M. Sigaud, and E. C. Montenegro, Phys. Rev. A **63**, 062717 (2001).
[14] J. A. Tanis, E. M. Bernstein, M. W. Clark, S. M. Ferguson, and R. N. Price, Phys. Rev. A **43**, 4723 (1991).
[15] X. M. Chen, Y. X. Lu, Z. M. Gao, Y. Cui, Y. W. Liu, and J. Du, Nucl. Instrum. Methods Phys. Res. B **262**, 161 (2007).
[16] J. X. Shao, X. M. Chen, Z. Y. Liu, R. Qi, and X. R. Zou, Phys. Rev. A **77**, 042711 (2008).
[17] B. W. Ding, X. M. Chen, H. B. Fu, G. Z. Sun, J. X. Shao, and Z. Y. Liu, Int. J. Mass Spectrom. **270**, 47 (2008).
[18] X. R. Zou, J. X. Shao, X. M. Chen, Y. Cui, Z. M. Gao, Y. Z. Yin, B. W. Ding, Z. Li, and D. Y. Yu, Phys. Rev. A **80**, 052701 (2009).
[19] J. H. McGuire, Adv. At. Mol. Opt. Phys. **29**, 217 (1991).
[20] A. B. Voitkiv and A. V. Koval, J. Phys. B **29**, 2661 (1996).
[21] M. M. Sant'Anna, E. C. Montenegro, and J. H. McGuire, Phys. Rev. A **58**, 2148 (1998).
[22] T. Kirchner, H. J. Lüdde, and R. M. Dreizler, Phys. Rev. A **61**, 012705 (1999).
[23] T. Kirchner, H. Tawara, I. Yu. Tolstikhina, A. D. Ulantsev, V. P. Shevelko, and Th. Stöhlker, Tech. Phys. **51**, 1127 (2006).
[24] A. D. Ulantsev, J. Phys. B **41**, 165203 (2008).
[25] E. G. Cavalcanti, G. M. Sigaud, E. C. Montenegro, M. M. Sant'Anna, and H. Schmidt-Böcking, J. Phys. B **35**, 3937 (2002).
[26] E. G. Cavalcanti, G. M. Sigaud, E. C. Montenegro, and H. Schmidt-Böcking, J. Phys. B **36**, 3087 (2003).
[27] M. M. Sant'Anna, H. Luna, A. C. F. Santos, C. McGrath, M. B. Shah, E. G. Cavalcanti, G. M. Sigaud, and E. C. Montenegro, Phys. Rev. A **68**, 042707 (2003).
[28] G. M. Sigaud, M. M. Sant'Anna, H. Luna, A. C. F. Santos, C. McGrath, M. B. Shah, E. G. Cavalcanti, and E. C. Montenegro, Phys. Rev. A **69**, 062718 (2004).
[29] T. Spranger and T. Kirchner, J. Phys. B **37**, 4159 (2004).
[30] M. E. Galassi, R. D. Rivarola, and P. D. Fainstein, Phys. Rev. A **75**, 052708 (2007).
[31] A. Russek and M. T. Thomas, Phys. Rev. **109**, 2015 (1958).
[32] C. L. Cocke, Phys. Rev. A **20**, 749 (1979).

[33] J. H. McGuire, N. Stolterfoht, and P. R. Simony, Phys. Rev. A **24**, 97 (1981).
[34] N. M. Kabachnik, V. N. Kondratyev, Z. Roller-Lutz, and H. O. Lutz, Phys. Rev. A **56**, 2848 (1997).
[35] C. D. Archubi, C. C. Montanari, and J. E. Miraglia, J. Phys. B **40**, 943 (2007).
[36] D. R. Schultz, R. E. Olson, C. O. Reinhold, S. Kelbsch, C. Kelbsch, H. Schmidt-Böcking, and J. Ullrich, J. Phys. B **23**, 3839 (1990).
[37] J. Fiol, R. E. Olson, A. C. F. Santos, G. M. Sigaud, and E. C. Montenegro, J. Phys. B **34**, L503 (2001).
[38] R. E. Olson, R. L. Watson, V. Horvat, A. N. Perumal, Y. Peng, and Th. Stöhlker, J. Phys. B **37**, 4539 (2004).
[39] K. Riesselmann, L. W. Anderson, L. Durand, and C. J. Anderson, Phys. Rev. A **43**, 5934 (1991).
[40] G. M. Sigaud, J. Phys. B **41**, 015205 (2008).
[41] P. L. Grande, G. Schiwietz, G. M. Sigaud, and E. C. Montenegro, Phys. Rev. A **54**, 2983 (1996).
[42] A. B. Voitkiv, G. M. Sigaud, and E. C. Montenegro, Phys. Rev. A **59**, 2794 (1999).
[43] A. B. Voitkiv, N. Grün, and W. Scheid, J. Phys. B **33**, 3431 (2000).
[44] T. Kirchner and M. Horbatsch, Phys. Rev. A **63**, 062718 (2001).
[45] T. Kirchner, H. J. Lüdde, and M. Horbatsch, Phys. Scr. **T110**, 364 (2004).
[46] T. Kirchner, Nucl. Instrum. Methods Phys. Res. B **233**, 151 (2005).
[47] E. S. Solov'ev, R. N. Il'in, V. A. Oparin, and N. V. Fedorenko, Zh. Eksp. Teor. Fiz. **42**, 659 (1962) [Sov. Phys. JETP **15**, 459 (1962)].
[48] S. Wexler, J. Chem. Phys. **41**, 1714 (1964).
[49] L. J. Puckett and D. W. Martin, Phys. Rev. A **1**, 1432 (1970).
[50] H. K. Haugen, L. H. Andersen, P. Hvelplund, and H. Knudsen, Phys. Rev. A **26**, 1950 (1982).
[51] H. K. Haugen, L. H. Andersen, P. Hvelplund, and H. Knudsen, Phys. Rev. A **26**, 1962 (1982).
[52] R. D. DuBois, L. H. Toburen, and M. E. Rudd, Phys. Rev. A **29**, 70 (1984).
[53] J. H. McGuire, A. Müller, B. Schuch, W. Groh, and E. Salzborn, Phys. Rev. A **35**, 2479 (1987).
[54] L. H. Andersen, P. Hvelplund, H. Knudsen, S. P. Møller, A. H. Sørensen, K. Elsener, K.-G. Rensfelt, and E. Uggerhøj, Phys. Rev. A **36**, 3612 (1987).
[55] H. Berg *et al.*, J. Phys. B **25**, 3655 (1992).
[56] H. Knudsen, L. H. Andersen, P. Hvelplund, G. Astner, H. Cederquist, H. Danared, L. Liljeby, and K.-G. Rensfelt, J. Phys. B **17**, 3545 (1984).
[57] M. B. Shah and H. B. Gilbody, J. Phys. B **18**, 899 (1985).
[58] J. L. Forest, J. A. Tanis, S. M. Ferguson, R. R. Haar, K. Lifrieri, and V. L. Plano, Phys. Rev. A **52**, 350 (1995).
[59] R. D. DuBois, Phys. Rev. Lett. **52**, 2348 (1984).
[60] R. D. DuBois, Phys. Rev. A **33**, 1595 (1986).
[61] R. D. DuBois and S. T. Manson, Phys. Rev. A **35**, 2007 (1987).
[62] R. D. DuBois, Phys. Rev. A **36**, 2585 (1987).
[63] R. D. DuBois, Phys. Rev. A **39**, 4440 (1989).
[64] R. D. DuBois and L. H. Toburen, Phys. Rev. A **38**, 3960 (1988).
[65] O. Woitke, P. A. Závodszky, S. M. Ferguson, J. H. Houck, and J. A. Tanis, Phys. Rev. A **57**, 2692 (1998).
[66] M. Saito, Y. Haruyama, N. Hamamoto, K. Yoshida, A. Itoh, and N. Imanishi, J. Phys. B **28**, 5117 (1995).
[67] T. Tonuma, H. Kumagai, T. Matsuo, and H. Tawara, Phys. Rev. A **40**, 6238 (1989).
[68] H. Tawara, T. Tonuma, H. Kumagai, and T. Matsuo, Phys. Rev. A **41**, 116 (1990).
[69] T. Matsuo, T. Tonuma, H. Kumagai, and H. Tawara, Phys. Rev. A **50**, 1178 (1994).
[70] E. C. Montenegro and W. E. Meyerhof, Phys. Rev. A **43**, 2289 (1991).
[71] E. C. Montenegro, A. C. F. Santos, W. S. Melo, M. M. Sant'Anna, and G. M. Sigaud, Phys. Rev. Lett. **88**, 013201 (2001).
[72] A. C. F. Santos, W. S. Melo, M. M. Sant'Anna, G. M. Sigaud, and E. C. Montenegro, Rev. Sci. Instrum. **73**, 2369 (2002).
[73] W. Wolff, H. Luna, A. C. F. Santos, E. C. Montenegro, and G. M. Sigaud, Phys. Rev. A **80**, 032703 (2009).
[74] M. M. Sant'Anna, W. S. Melo, A. C. F. Santos, M. B. Shah, G. M. Sigaud, and E. C. Montenegro, J. Phys. B **33**, 353 (2000).
[75] H. Knudsen, H. K. Haugen, and P. Hvelplund, Phys. Rev. A **23**, 597 (1981).
[76] E. C. Montenegro, K. L. Wong, W. Wu, P. Richard, I. Ben Itzhak, C. L. Cocke, R. Moshammer, J. P. Giese, Y. D. Wang, and C. D. Lin, Phys. Rev. A **55**, 2009 (1997).
[77] E. C. Montenegro, W. E. Meyerhof, and J. H. McGuire, Adv. At. Mol. Opt. Phys. **34**, 250 (1994).
[78] D. H. Crandall, R. A. Phaneuf, B. E. Hasselquist, and D. C. Gregory, J. Phys. B **12**, L249 (1979).
[79] M. Mattioli, G. Mazzitelli, M. Finkenthal, P. Mazzotte, K. B. Fournier, J. Kaastra, and M. E. Puiatti, J. Phys. B **40**, 3569 (2007).
[80] S. M. Younger, J. Quant. Spectrosc. Radiat. Transfer **26**, 329 (1981).
[81] E. C. Montenegro and T. J. M. Zouros, Phys. Rev. A **50**, 3186 (1994).
[82] M. R. C. McDowell and J. P. Coleman, *Introduction to the Theory of Ion-Atom Collisions* (North-Holland, New York, 1970).
[83] H. A. Bethe and R. Jackiw, *Intermediate Quantum Mechanics*, 2nd ed. (Benjamin, Reading, 1968), Chap. 17.
[84] G. P. Williams, *X-Ray Booklet*, 2nd ed. (Lawrence Berkeley National Laboratory, Berkeley, 2001)
[85] M. E. Rudd, Y.-K. Kim, D. H. Madison, and J. W. Gallagher, Rev. Mod. Phys. **57**, 965 (1985).